Multimodal *Operando* Analysis of Lithium Sulfur Multilayer Pouch Cells: An In-depth Investigation on Cell Component Design and Performance

Rafael Müller[a]*, Tom Boenke[b,c], Susanne Dörfler[b], Thomas Abendroth[b], Paul Härtel[b], Holger Althues[b], Stefan Kaskel[b,c], Nikolay Kardjilov[a], Henning Markötter[d], Michael Sintschuk[d], André Hilger[a], Ingo Manke[a], Sebastian Risse[a]*

[a] Institute for Electrochemical Energy Storage, Helmholtz-Zentrum Berlin, Hahn Meitner Platz 1, 14109 Berlin, Germany

[b] Fraunhofer IWS, Winterbergstraße 28, 01277 Dresden, Germany

[c] Technische Universität Dresden, Inorganic Chemistry I, Bergstr. 66, 01069 Dresden, Germany

[d] Bundesanstalt für Materialforschung und -Prüfung, 12205 Berlin, Germany

* Corresponding Authors: rafael.mueller@helmholtz-berlin.de & sebastian.risse@helmholtz-berlin.de

Keywords: lithium sulfur batteries, multimodal operando analyses, x-ray imaging, impedance spectroscopy, multilayer pouch cells, current collector perforation

GRAPHICAL ABSTRACT

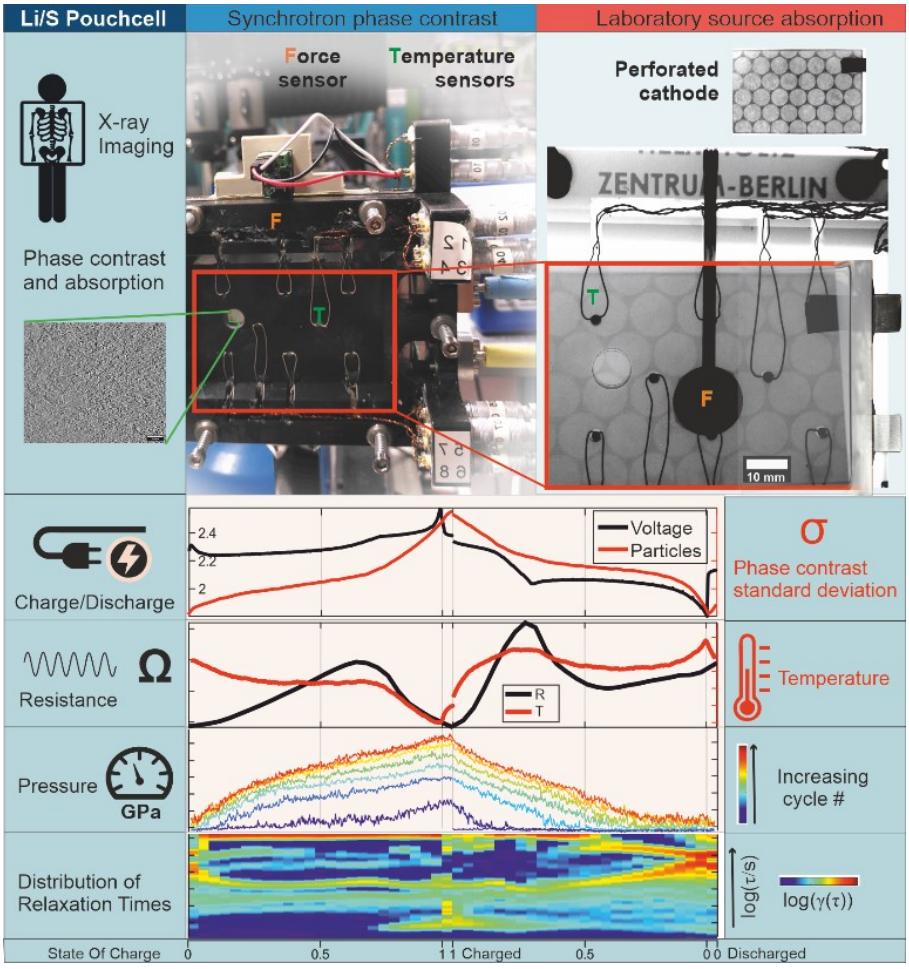

TOC-Figure: Overview of voltage, force, temperature, resistance, DRT, and image data.

ABSTRACT

This study presents an innovative operando analysis of lithium-sulfur (Li/S) multilayer pouch cells, employing a combination of lab-source and synchrotron X-ray imaging to investigate sulfur crystallite dissolution and lithium dendrite formation. By integrating advanced X-ray imaging, impedance spectroscopy, and simultaneous monitoring of temperature and pressure, the research uncovers critical insights into the behavior of active and inactive cell components. The analysis reveals significant degradation increments, primarily driven by side product accumulation and the deterioration of lithium microstructures, which contribute to performance loss over cycling. Additionally, temperature distribution analysis shows a strong correlation between joule heating, polarization resistance, and the observed endothermic processes during crystallization. These findings provide a comprehensive understanding of the mechanistic processes within industrially relevant pouch cells, highlighting opportunities for optimizing Li/S cell designs and advancing high-energy-density battery systems for commercial applications.

Introduction

Lithium-sulfur (Li/S) batteries have shown great promise as an emerging sustainable energy storage technology. They not only utilize abundant raw materials but also boast a remarkable theoretical specific energy of approximately 2500 Wh/kg. Prototype cells already achieve up to 500 Wh/kg, almost twice the specific energy of current lithium-ion batteries.[1] This high energy density is a significant advantage for non-stationary electric devices, mainly aerial applications. Despite these advantages, the Li/S battery chemistry is prone to severe degradation effects. These include issues like the notorious shuttle effect[2], which involves the dissolution of polysulfides into the electrolyte and their subsequent transportation to the anode, causing efficiency loss. Additional challenges are the 'dry-out' problem of the electrolyte and the cyclical increase of inactive sulfur phases due to side reactions, further impeding battery performance. A comprehensive understanding of these mechanistic processes and degradation pathways is thus of utmost importance, as it holds the key to devising improved cell concepts and overcoming these challenges.

Preliminary measurements and investigations at the coin cell level are essential for understanding novel lithium-sulfur cell concepts and their potential behavior. However, to truly achieve significant breakthroughs in the commercialization of lithium-sulfur technology, evaluating these cell chemistries within industrially relevant cell formats is mandatory.[3] These

include pouch cells, cylindrical cells, and prismatic cells. These formats better emulate real-world use-case scenarios and reveal the inherent complexities of cell performance at a larger scale. The processes within these cells are intricate, making it even more challenging to decipher their exact behavior. Thus, the use of multimodal operando methods becomes vitally important. These methods allow for simultaneous measurements from multiple perspectives and provide correlated insights into the mechanistic interplay of processes within the operating cell. X-ray imaging offers a high penetration through battery materials for visualizing internal structures and interfaces, including electrodes and separators. Real-time imaging capability enables monitoring of dynamic processes and changes within the battery during operation.

While Li/S batteries naturally exhibit high energy density, further optimization potential lies in minimizing the weight of inactive cell components. These include the current collectors and the electrolyte, which do not directly contribute to energy storage. However, the real impact of such weight-reducing measures on overall cell performance is yet to be thoroughly investigated. The challenge here lies in assessing the trade-off between reduced weight and maintained performance. In this context, X-ray imaging techniques prove to be incredibly valuable.[4–7] Sulfur forms macroscopic crystals in the charged state, which can be efficiently imaged with incoherent laboratory X-ray sources. This allows for a detailed study of the sulfur phase precipitation to probe the dependence on the current collector design. In addition, the lithium plating and stripping process, another crucial aspect of Li/S battery operation, can be ideally studied using phase-contrast X-ray imaging at a coherent synchrotron source.[8] This technique reveals phase boundaries and emphasizes edges while offering enhanced resolution to provide detailed imaging of fine structures and subtle changes in battery components, such as electrode wetting and dendrite formation. Thus, the major deposition products on both electrodes have been characterized, offering a unique view of the working cell's internal processes.

Our study examines pouch cells which comprise an innovative design (**Figure 1**): A perforated current collector on the cathode side and free-standing lithium metal anodes. These cells have an electrolyte-to-sulfur ratio of 5 µL per mg of sulfur, a design aimed at maintaining high energy density. Using a combination of different operando characterization techniques, including temperature distribution measurements, force measurements using a sensitive capacitor sensor, distribution of relaxation times from operando impedance spectroscopy, charge/discharge cycling analysis, and X-ray imaging, we were able to gain substantial insights into the pouch cell's behavior. The results provide an extensive picture of how different components and factors interact within the cell during operation. These findings not only enhance our

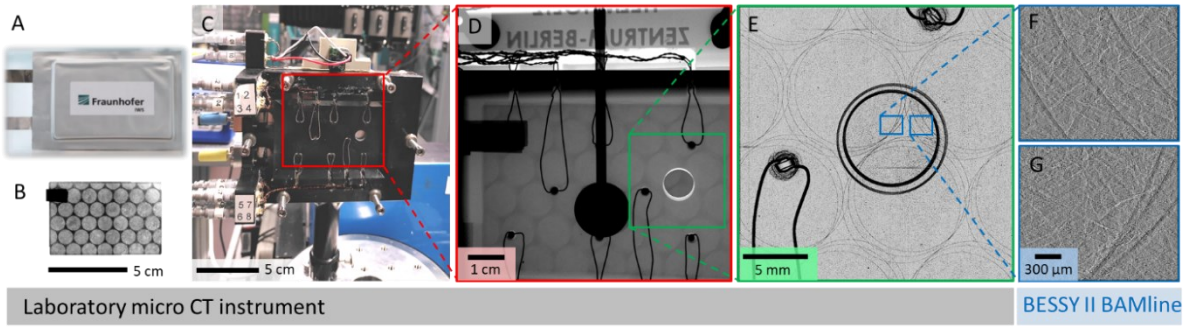

Figure 1: A) Photo of a 46 x 71 mm type pouch cell. B) Radiography of the electrode stack within the pouch cell. C) Photo of the multimodal operando pouch cell setup mounted at the Bessy II BAMline beamline. D) Radiography from the laboratory µCT of the full pouch cell within the operando holder. E) Radiography of the region around the drilling in the holder with higher magnification and rolling ball background subtraction. F) Phase contrast radiographs from the BESSY II BAMline of the main dose and low dose (G) spots.

understanding of the lithium-sulfur technology at a commercial scale but also help identify potential opportunities for further optimization of commercially relevant cell formats.

1. Experimental

1.1. Electrode and Pouch Cell Preparation

The multi-layered pouch cells were provided by Fraunhofer IWS using the following methods:

Cathode manufacturing

Boenke et al.[9] previously reported cathode manufacturing with freestanding CNT Buckypaper, sulfur, and a perforated current collector. The process was carried out by a sulfur transfer melt infiltration technique of commercial CNT Buckypaper (1.0 mg/cm², 75M25C, MWCNT Buckypaper, NTL) at 155 °C for 1 h. The freestanding cathodes with the final dimensions of 46 x 71 mm² were laminated at 90 °C onto the primer-coated perforated aluminum foil (20 µm, MTI).

The aluminum current collector foils were prepared with a laser cutting system developed at Fraunhofer IWS. A circular cutting pattern was specifically designed to mimic a hexagonal honeycomb structure, with each hole having a 9 mm diameter and a 10 mm center-to-center distance. This method reduced the overall weight of the current collector foil by 80 %.

For the pouch cell assembly, a cathode sulfur loading of 1.2 ± 0.1 mg-S/cm² (53 ± 1 wt % sulfur) was selected. The total thickness of the cathodes, including the current collector, was 90 ± 5 µm, and the electrode density was 0.60 ± 0.05 g/cm³. Details of the resulting cell parameters are summarized in the SI Table 1.

Electrolyte

The DME/DOL electrolyte system consisted of 1 M LiTFSI (lithium bis(trifluoromethyl-sulfonyl)imide), 99.95 %, anhydrous, Gotion) and 0.5 M $LiNO_3$ (lithium nitrate, 99.98 %, anhydrous, Alfa Aesar) in a mixture (1:1, v/v) of DME (1,2-dimethoxy ethane, 99.99 %, Gotion) and DOL (1,3-dioxolane, 99.99 %, Gotion). LiTFSI and $LiNO_3$ were dried at 120 °C for 12 h in vacuum. The sulfur-loaded cathodes were vacuum-dried for 12 h at room temperature and 1 h at 50 °C. All solvents were purified by threefold molecular sieve extraction (3 Å).

Pouch cell assembly

Three double-sided cathodes (46 x 71 mm²) were stacked with four pure lithium anodes (2 x 50 µm Li from CEL China Energy, 50 µm thick, 46 x 71 mm², copper flag) and separated by a 12 µm thick polyethylene separator foil. The cells were filled with the DME/DOL electrolyte to achieve an electrolyte/sulfur ratio of 5.0 ± 0.5 µL/mg-S. The cells were sealed under vacuum into a 111 µm thick pouch foil. The cell holder was an improved version of the setup developed by Müller et al.[10]

1.2. Multimodal Operando Measurements

Our selection of x-ray methods encompasses lithium dendrite detection with phase contrast imaging and sulfur particle detection by µCT. The quantitative detection of Li_2S is not possible for the required conditions and is an ongoing challenge. XRD methods have been used to qualitatively confirm its presence as nanoparticles, but amorphous amounts of Li_2S may well elude that method. X-ray spectroscopic methods have been applied to follow the Li_2S formation, but require dedicated experimental design which is poorly suitable for pouch cell analysis. [1,2]

Multimodal setup

The 3D-printed multimodal operando cell holder was specifically designed for the 46 mm x 71 mm electrode pouch cell dimensions (Fig. 1C). Eight negative-temperature-coefficient (NTC) temperature sensors (44031RC precision thermistor, Measurement Specialties INC.) have been embedded inside cavities on the front panel to circumvent indentations. The individual sensor offset was less than 0.5 °C and the measured noise around 0.05 °C. An additional reference temperature sensor was incorporated at the outer frame to subtract ambient temperature fluctuations and provide accurate cell temperature readings. A highly sensitive,

capacitive force sensor (15 mm ⌀, 4.5 N, SingleTact) was mounted centrally on the backside of the pouch cell to monitor the force evolution during cycling (Fig. 1D). The setup was used to set an initial force on the cell optimized for the most sensitive available sensor (up to 4.5 N). The force sensor allows the monitoring of the force on the complete pouch cell encompassing superimposed contributions of anode, cathode and filling medium. For optimal imaging contrast with the incoherent lab source, the cell holder was crafted from a low-attenuation polymer by 3D printing. Nevertheless, a 5 mm hole (Fig. 1E) was drilled into the back and front holder frames to avoid their background signal contribution during synchrotron X-ray imaging. Six adjustable screws and springs held the frames together with the pouch cell between them. The resulting pressure on the cell ranged around 1 kPa and is intended to monitor the dimensional change and not introduce compaction, as tested by Schmidt et al. with 0.3 MPa.[11]

X-ray imaging

The phase contrast imaging experiments at the BAMline[4,12] of Bessy II were conducted using a monochromatic photon beam energy of 25 keV with the W/Si double multilayer monochromator offering an energy resolution (ΔE/E) of ~3-4%. Images were recorded with an Optique-Peter microscope and a PCO.edge 5.5 sCMOS camera using a lens system resulting in an effective pixel size of 0.72 µm offering a field of view of 1.8×1.5 mm². Sample-detector distance was set to 400 mm for optimal balance between phase contrast and image blurring. Considering an estimated effective source size of a few hundred µm ~35 m upstream,[12] results in a blurring and limits the resolution to ~2.5 µm. There is no noticeable further reduction of the resolution due to the pixel size of 0.7 µm. To verify that monitoring of battery cycling over a long period of time with hard X-Rays remained non-invasive, two locations were monitored with different exposure times. The main spot had 15 times longer exposure than the secondary spot. The main “high-dose” spot showed the same mechanistic behavior as the “low-dose” spot with minimized radiation exposure, and thus, beam influence can be assumed as absent unless an unlikely dose-independent exposure impact is present. The examination of the exposed area in the µCT radiography after the synchrotron experiments did not indicate beam damage either. The pouch cells were assembled by IWS-Dresden and transferred to HZB on the same day. On the starting day of the beam-time, a cell was placed in the setup and held at open circuit potential until the start of cycling. No further preconditioning was applied.

Image analysis

The system being studied, a multilayer pouch cell, presents significant challenges for detecting and evaluating electrode-specific morphologies due to the inherent superposition of signals from the whole cell in transmission radiography images. To extract a simplified image descriptor, we analyzed the imaging data from the BAMline and µCT X-ray sources using image normalization and enhancing methods. After conventional image flatfield and darkfield normalizations and registration, we tracked the development of internal structures over time by calculating the standard deviation of pixel values across individual X-ray images. Each image from a given experimental series was standardized by dividing it by the median pixel value of all images in that series (referred to as Static Median or StatMed). Secondly, we assessed changes in these structures using a sliding image processing technique, comparing the median pixel value of a small, central group of images to that of a broader surrounding time series (referred to as Moving Median or MovMed). The standard deviation of these processed images provided a measure of the rate of structural changes. The more difference an image contains compared to the respective median image, the higher the standard deviation value.

In the experiments, we utilized both an incoherent laboratory X-ray source and a coherent synchrotron source, which allowed us to observe different structures separately. The synchrotron source is particularly effective at highlighting dendritic lithium structures in the projected X-ray image due to their strong phase contrast. In a complementary way, sulfur species absorb X-rays strongly and are more prominently observed with the laboratory source, where lithium dendrites are barely resolved.

Cell cycling and further operando measurements

The cell was cycled with a C-rate of C/5 within a voltage window of 1.8 V to 2.8 V. Deploying a customized impedance spectroscopy script, continuous monitoring of charge transfer processes was enabled, yielding around 150 EIS spectra in each charge and discharge step. The applied AC voltage amplitude was maximally 10 mV (rms), and the maximum AC current amplitude (rms) was C/50. The frequency range spanned from 250 kHz to 250 mHz with ten points per decade. Resultant EIS spectra were corrected using a drift correction algorithm and fitted using a distribution of relaxation times model.

During the operando measurements at the BAMline, a Keithley DAQ6510 multimeter continuously recorded the NTC thermistor and force sensor readings.

2. Results and Discussion

2.1. Multimodal operando measurement

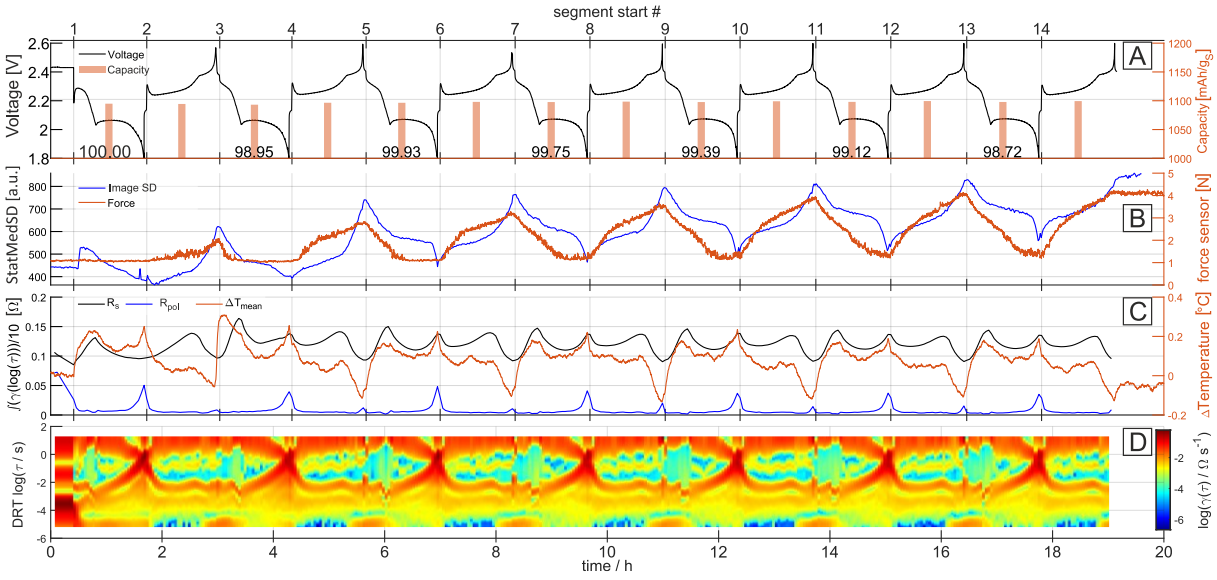

Figure 2 shows all collected correlated results of the multimodal operando measurements. The timeline is given, and a vertical grid indicates the charge-discharge cycle switches. A SoC

normalized overlay of the data is attached as

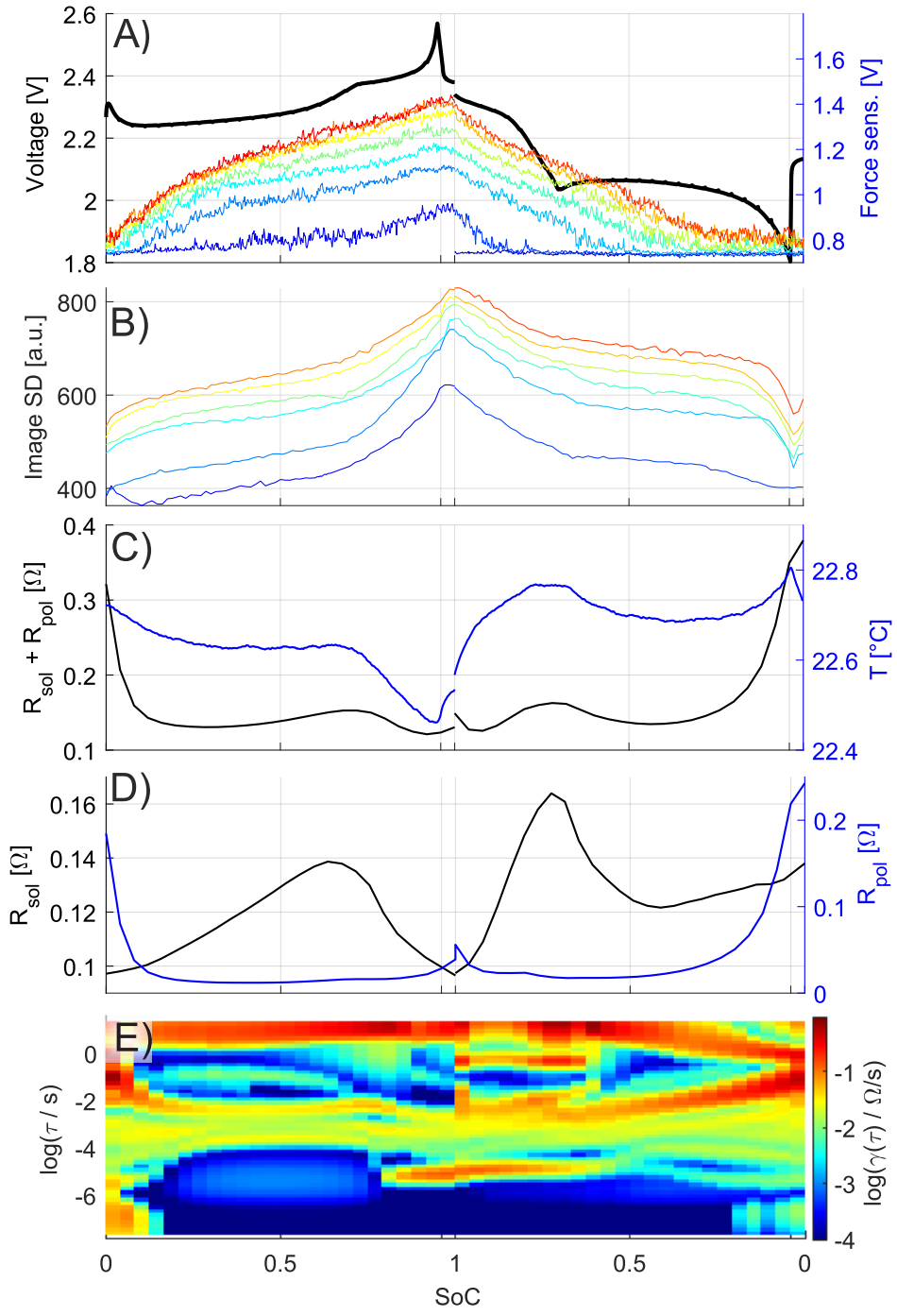

Figure S6. The voltage curve closely resembles the expected ex-situ behavior of reference cells and the results from[9]. The voltage during discharge exhibits a first downward sloped plateau, a local minimum "voltage dip", and a longer second discharge plateau. The charging voltage curve starts with an overpotential spike and rises steadily afterward. It exhibits a first long plateau (to 2.3 V) and a short second plateau until 2.4 V. At the end of each respective charge and discharge segment, a potentiostatic EIS was recorded. The voltage curve relaxes to OCP during these few minutes of measurement time. The radiography image pixel standard deviation

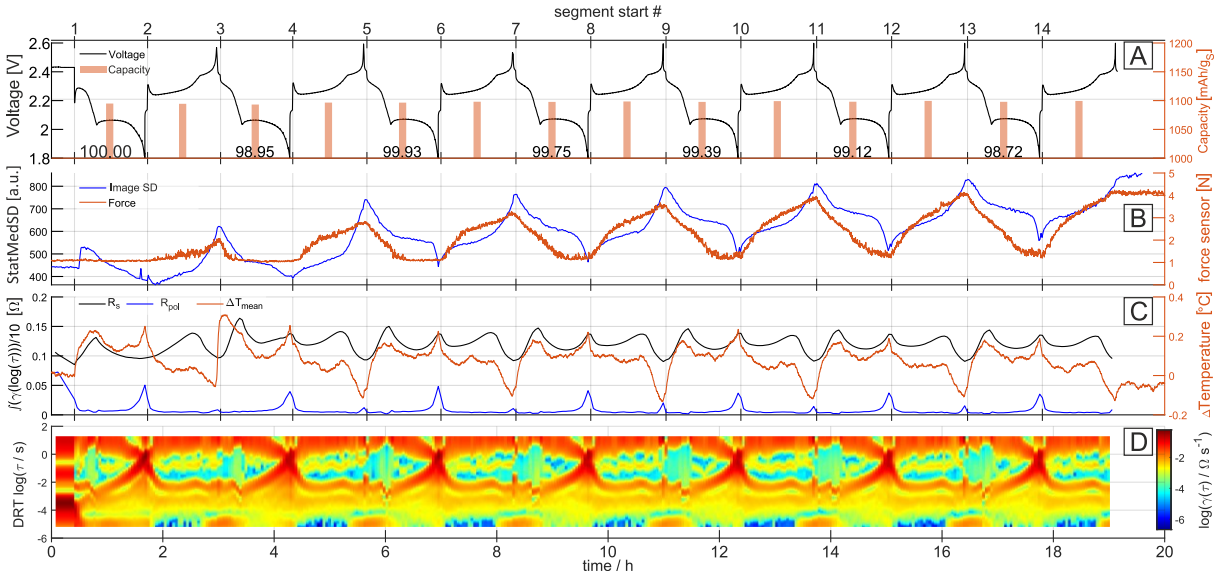

Figure 2: Summary of the multimodal operando measurements: A) Left y-axis: Voltage. Right y-axis capacity bars. Inset values: Discharge Coulomb efficiency based on the prior charge. B) Left y-axis: Phase contrast radiography image standard deviation (SD). This indicates the extent of phase boundaries and represents the amount of particles and dendrites. Right y-axis: Pressure sensor readings C) Left y axis: Solution Resistance R_s and Polarization resistance R_{pol} from EIS fitting. Right y-axis: Temperature sensor response deviation from initial temperature. D) Distribution of relaxation times (DRT) from EIS fitting.

(SD, see **Figure S3** and sections 2.4 and 2.5 for details) obtained after static median pseudo-flatfield image normalization (StatMedSD) reflects the global relative presence of phase boundaries. A low StatMedSD means the normalized image is more homogeneous and contains fewer phase contrast features. High StatMedSD values mean the normalized image is rich in contrasts, dominated by the multiple and spread phase edges of mossy lithium dendrites and sulfur crystallites. The superimposed formation of these species can be seen in the different slope regimes of the StatMedSD curve. The initial jump at the beginning of the first discharge is caused by the wetting and dissolution of the alpha sulfur crystals. During the first discharge, the StatMedSD reaches an absolute minimum, where the initial lithium surface stripping and pitting structure is formed. This structuring is largely maintained during the full experiment time, and thus, the pseudo-flatfield normalization minimizes its contribution to the resulting StatMedSD. The pitting spots give rise to preferred lithium deposition regions, likely due to a weakened passivation layer.[8,13] A steady, slow rise is observed during charging, followed by a steeper rise when the dendritic lithium and sulfur crystallite growth occurs together.[14]

The reverse trend is visible for the discharge cycle. The initial low StatMedSD values are not reached at the end of discharge for the following cycles, which indicates an accumulation of irreversible structuring and inactive lithium remains, as found by other groups in in-situ and ex-

situ studies with X-ray tomography and SEM [15,16,17,8]. As a new feature, a sharper minimum evolves at the discharged state, and image comparison suggests that almost all lithium dendrites are stripped at this stage, see Figure 5.

The force readings exhibit increasing maxima at the charged state and fall back to a baseline force level in the discharged state. The baseline force equals the initial charged pressure level of the setup. It does not drop during the first discharge, indicating the minimum measurable cell expansion state. This constant baseline can be explained by the rigidness of the pouch cell body, especially the sides, which do not allow further compression but can account for buffering of irreversible processes to some extent. An irreversible accumulation of (gaseous) side products by electrolyte decomposition could lead to incremental pressure build-up with consecutive cycles, explaining the rise of the maxima.[18–20] Extended cycling might give rise to increasing expansion minima, as seen by Waluś et al.[21]

The pressure curve during one cycle behaves monotonously, showing different slope regions and a lower plateau. The pressure curve initially rises steeply upon charging, and then the slope declines. During discharge, the pressure drops rapidly and then approaches the lower plateau. This is expected when the volumetric changes of both electrodes are considered, as the volume of lithium and sulfur combined is larger than that of the reaction product lithium sulfide. The often-described 80% volume change of the cathode [22] does not dictate the overall behavior, which is governed by lithium deposition and stripping.[13]

Furthermore, the overall force arriving on the force sensor depends not only on the ideal chemical conversion of the active materials ($2\ Li + S \rightarrow Li_2S$) but also on their distribution and intermediate phases (solid or dissolved and elemental or compounded). The density of the electrolyte changes with the formation of various polysulfide species and clustering behavior. Additionally, anisotropic morphological effects like the push of dendritic growth may not entirely be disregarded.[23,24] Wood et al.[13] describe different lithium growth processes that may explain the steeper force slope at the beginning of charge and discharge. The vertical lithium growth can push against the separator in compact pouch cells and then turn to lateral and bulk growth. Similar behavior of lithium dendrites has been reported by Sadd et al.[8]. Steiger et al.[25–27] describe mossy lithium growth starting from filaments. This mechanism is supported by the lateral motion of mossy lithium dendrite bushels, which is detectable as the concerted movement of radiography image patterns obtained near the charged state. See further details in the discussion of radiography images in section 2. Nevertheless, the shape of force evolution and the increasing maxima with cycle number are good reasons to apply more sensitive dilatometry to investigate this crucial property of industrial relevance.[22,28,29]

The simplest model for cell volume variation is the consideration of solid reaction products only and a steady linear transformation. This model would result in a triangular volume curve. A more realistic model would include densities of dissolved polysulfide species and solution equilibria for sulfur and lithium sulfide. With the combination of computational and experimental electrolyte density details, a comprehensive mechanistic model should be reachable to precisely predict the main reactions' expansion and thermal behavior.[30,31]

The solution resistance (R_s) is a figure of merit that indirectly reflects electrolyte properties such as viscosity and concentration of polysulfides (PS) and lithium.[32,33] The observed R_s maxima at the transition between the first and second voltage plateaus can be attributed to a high long-chain PS concentration.[34] This causes a rise in viscosity that hampers electrolyte conductivity. An additional maximum in the discharged state appears after the first charge and might be correlated to lithium surface SEI resistance after the reaction with polysulfides. The impedance of relaxation processes can be integrated to merge the resistive contributions to a polarization resistance (R_{pol}). Both resistances appear to contribute to coulomb heating.

The temperature is correlated to the ohmic drop contributions of both resistances R_s and $R_{pol.}$ Joule heating appears to be the strongest factor determining heat generation. The temperature curve shows a sharp rise at the beginning and end of the discharge, while cooling is observed during charging. The first discharge shows a rise and peak of temperature, while no inner resistance maximum is observed in the first discharged state in contrast to the following discharge states. This could indicate the contribution of reversible entropic heat effects related to the thermodynamics of phase transformations (i.e., lattice enthalpy contributions of crystallization and dissolution processes).[31–33]

The DRT shows a constant initial period during the OCP phase before the cell cycling, which indicates a stable unperturbed resting state in the operando setup. Upon the start of the first discharge, the DRT changes abruptly and exhibits a reproducible periodic pattern for the consecutive discharge/charge cycles. Three domains of high, medium, and low relaxation time regimes with different shifts of magnitude and time constant can be identified. The respective time ranges are low (10^{-7}-10^{-4} s), mid (10^{-4}-0.32 s), and high (0.32-20.1 s). Low relaxation time constants belong to fast processes, like electrode surface and double-layer polarization. Medium time constants typically are present for charge transfer processes, and high time constants determine diffusion processes.[35] The low-τ contribution decreases strongly during the beginning of the first discharge when the native lithium passivation layer is disrupted due to pitting and stripping. During charging, the low-τ contribution declines as quickly as the mid-τ

but passes a minimum and reaches another maximum towards the charged state. High-τ shows maxima near the transition of the plateaus, similar to the R_s and temperature curve maxima.

2.2. Degradation increment

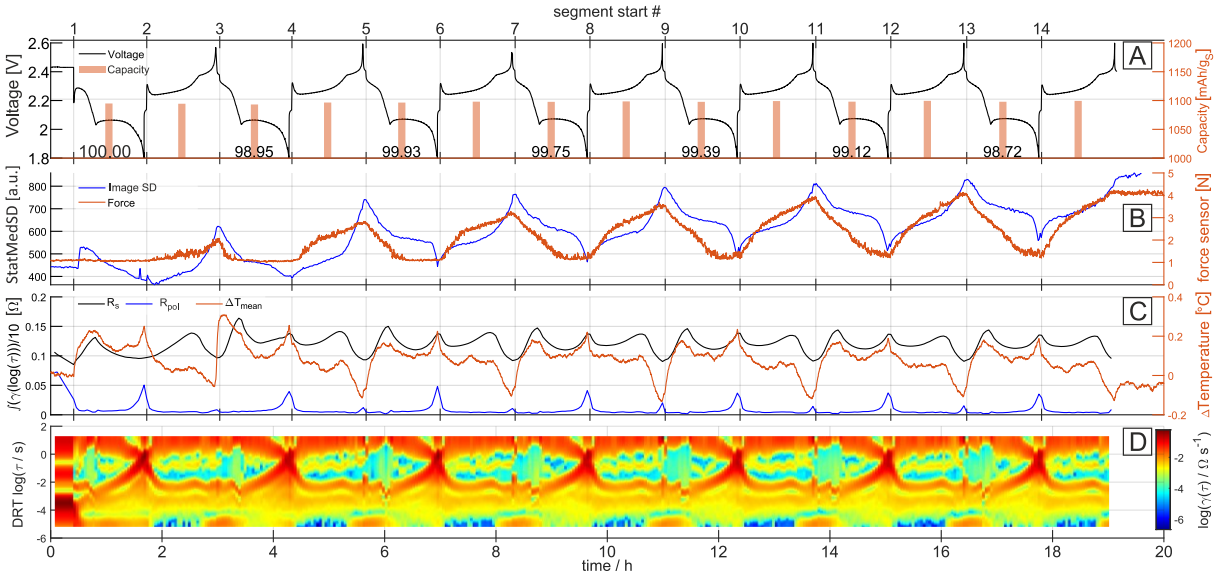

Figure **2** clearly illustrates the interdependencies from various cell characteristics through their time dependent correlation. Conversely, **Figure 3** depicts changes of crucial measurement parameters from one discharge-charge cycle to the next. To achieve this, parameter-time curves for each discharging and charging step were normalized to the state-of-charge (SoC). This normalization allows for comparisons between different cycle steps; for instance, values from the first charge step can be subtracted from those of the second (x-axis range 2.0 - 2.5). Such comparisons facilitate the detection of any increases or decreases in parameter values over successive cycles, thereby enabling the identification of SoC-dependent degradation increments. These increments offer insights into the timing of degradation mechanisms with respect to SoC. The graph aligns these measurements with the normalized voltage curves displayed at the top. Following this, the graph lists increments of degradation for various parameters in sequence from top to bottom: B) capacitance, C) overpotential ($\Delta\phi$), D) force (ΔF), E) standard deviation of radiographic images (ΔSD), F) solution resistance (ΔR_S), G) average temperature (ΔT), and H) the DRT ($\Delta\gamma$). The parameter increase and decrease are additionally highlighted by the filling colors red and green, respectively.

The relative capacity loss during the second discharge comes with an increase of solution resistance and charge transfer resistance (black arrow in panel H) and a distinct temperature rise at the beginning of the second voltage plateau. In the third discharge the capacity has increased showing a higher active material utilization. The relative temperature shows a reverse peak at the voltage dip along with a diminished solution resistance (green arrows). Afterwards

the cell converges to an increasingly stable state. An initial wetting and active material accessing process can explain the overall observations. This is relevant, as it shows the first "formation cycle" may not bring a cell to a steady cycling state, but additional cell "breathing" cycles may occur. The relative image standard deviation and relative force keep rising, but with lower magnitude per cycle. The curve for force increment (ΔF) exhibits a distinct, pulse-like increase in cell pressure, peaking around the charged state. Notably, the baseline pressure does not diminish throughout the entire cycling process. Consequently, the absence of incremental volume increasing processes, like gaseous side product accumulation, are indicated by the nearly zero force increment in the fully discharged state. Despite lithium sulfide (Li_2S) expanding by approximately 80% in the cathode relative to sulfur (S_8), it does not alone determine the overall pressure within the cell. The stripping and deposition processes occurring at the lithium metal anode dominate the overall cell's volume change due to the low density of lithium (Figure S8). This inference is supported by changes in the standard deviation (ΔSD), which reflects morphological alterations and is particularly responsive to the microstructures of lithium metal, especially in radiographic images captured in phase contrast mode. The presence of local minima in ΔSD at the cell's final states (100% SoC & 0% SoC) for the last four cycles suggests the ongoing formation of new microstructures within the imaged area.

The curve of solution resistance (ΔR_S) demonstrates a significant rise during the second discharge step, peaking concurrently with a voltage drop between the first and second discharge plateaus. At this precise point, the pouch cell also registers a higher average temperature than the previous discharge cycle. This increase in temperature can be attributed to a substantial release of polysulfides at this voltage level, which leads to a higher electrolyte viscosity and subsequently lowers its ionic conductivity. Concurrently, the charge transfer data shown in the ΔDRT graph indicates a marked rise in charge transfer in this region (black arrow in panel H). During the subsequent discharge step, the solution resistance falls again, accompanied by a decrease in temperature, suggesting a reduction in the concentration of polysulfides in the electrolyte. This reduction could be due to irreversible reactions involving reactive lithium microstructures at the anode. The observation supports this theory that the loss of active, cyclable sulfur results in an overpotential during the third discharge step across both voltage plateaus (2.0 – 2.5 on the x-axis, red arrows in panel C).

After the initial three cycles, the cell begins to stabilize progressively accompanied by a noticeable decrease in overpotential towards the end of the discharge step. This drop in overpotential closely aligns with a gradual shift in charge transfer resistance, particularly around relaxation times of approximately 0.1 seconds. This ongoing equilibration after cell

formation is particularly significant for industrial applications because it determines the long-term stability of the cell. The charge transfer resistance during this period can be attributed to two main factors: the reduction in the electrochemically active electrode surface area caused by lithium sulfide deposition at the cathode[36] and the loss of active sulfur inventory at the anode due to parasitic side reactions. In the anode case, the stripping process is possibly facilitated by a gradual disruption of the native passivation layer, leading to decreased activation energy.

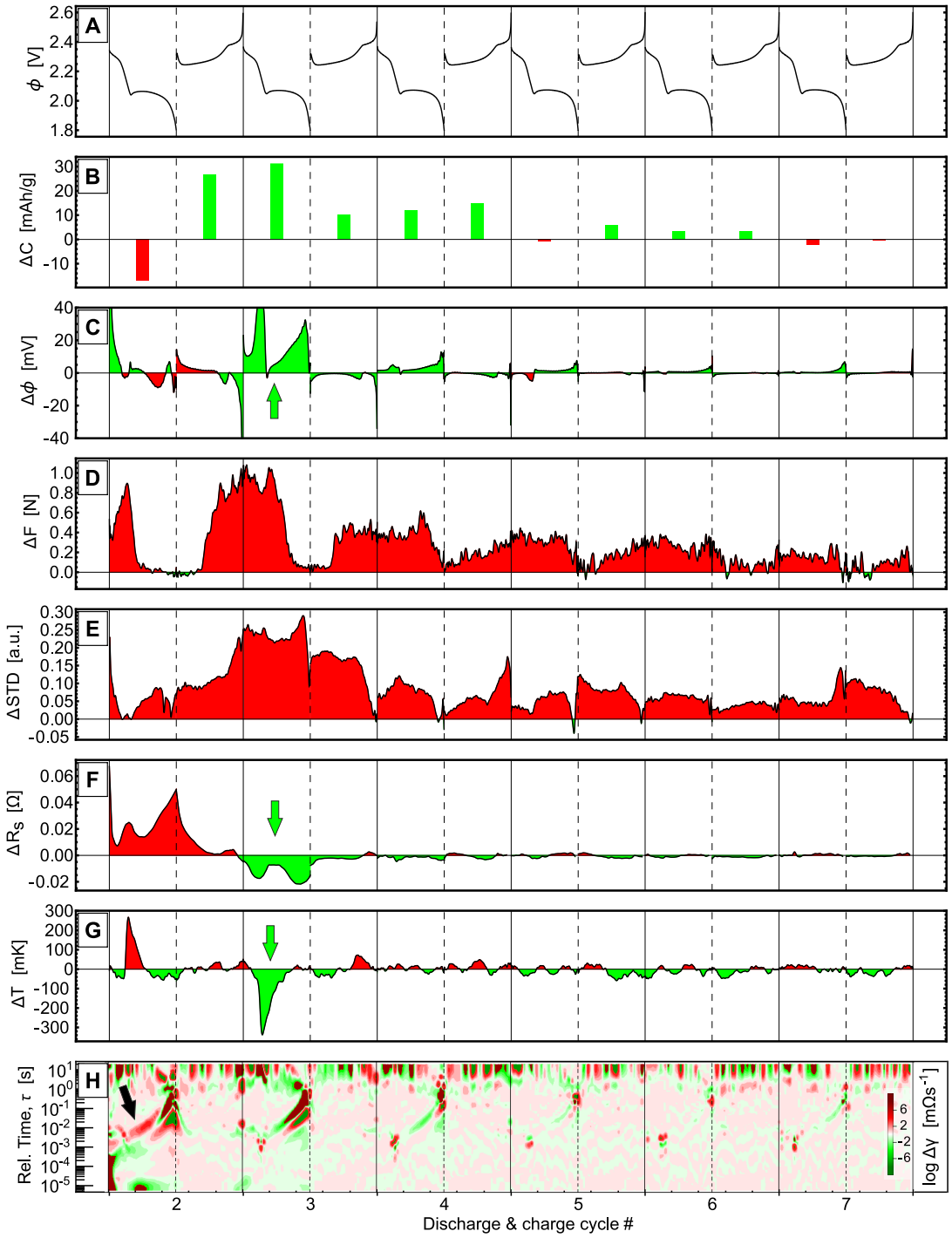

Figure 3: Degradation increment plots obtained by SoC normalization of all charge and discharge steps. The parameter values of the same SoC for two consecutive cycles were subtracted from each other to visualize the change of parameter values. A: Original voltage curve of the second of both cycles. B: Capacity change per cycle. C: Overpotential calculated from two consecutive cycles. D: Difference of the force parameter. E: Difference of the SD parameter reflecting morphology changes. F: Difference of the solution resistance. G: Difference of the average cell temperature. H: Difference in the charge transfer resistance.

2.3. Spatial temperature distribution

Due to the large surface area of pouch cells, understanding the temperature distribution during cycling is crucial for industrial applications. This information helps in designing battery management systems and cooling circuits. **Figure 4** displays the average temperature and voltage data for cycles 3-6. The parameter $\overline{\partial_t \Delta T}$ represents the average rate of temperature change in the cell (T_{cell}) relative to the outside temperature (T_{Out}), where $\Delta T = T_{cell} - T_{Out}$. Notably, the cell tends to heat up during charging phases (A & E) and cool down during discharging phases (C). Interestingly, the cell often begins to cool just before reaching a fully charged state (D), a point that coincides with the formation of sulfur crystals, possibly indicating an endothermic reaction during crystallization. Spatially, the temperature distribution shows that both cell tabs influence the heating rate, aiding the cell's cooling and heating. Furthermore, the maximum and minimum temperature rates are found near the cell's center due to thermal insulation. This insulation causes heat to be released slowly to the edges of the cell through conduction and radiation.

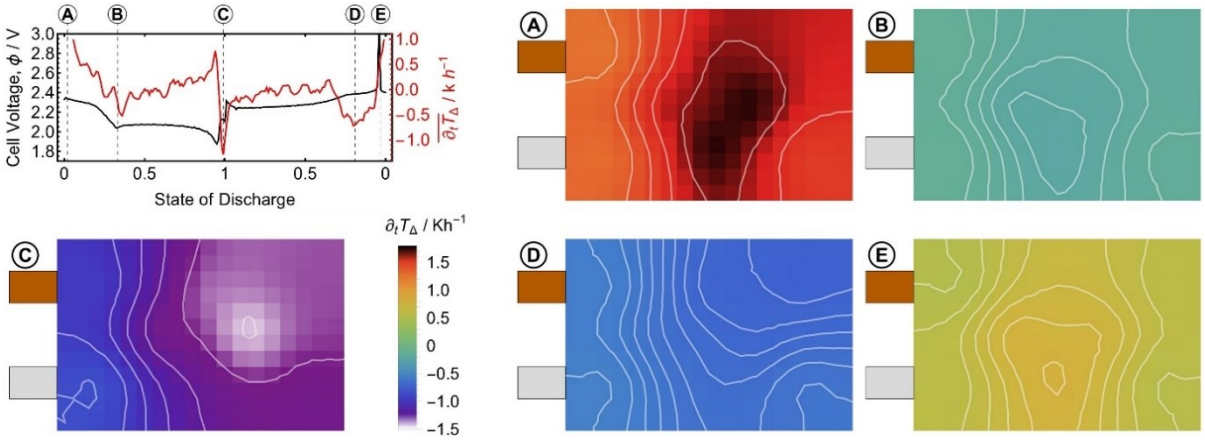

Figure 4: Temperature distribution of the pouch cell. Left upper corner: Averaged voltage (ϕ, black) and temperature rate ($\overline{\partial_t \Delta T}$, red) curve from cycles 3-6. Spatial averaged temperature distribution of the pouch cell measured with eight NTC thermistors.

2.4. Operando phase contrast radiography at the synchrotron

The initial crystallites of alpha sulfur [6] in the pouch cell were observed to be mostly around 10-50 µm in diameter with a few larger ones up to 100 µm, as shown in **Figure 5** (pristine). However, the occurrence of nanosized sulfur deposits on the cathode material, either within nanopores or as a thin layer on the carbon nanotubes (CNTs), cannot be ruled out. The distribution of these macroscopic crystallites was uneven and was assessed by examining two specific areas. During the first cycle, these alpha sulfur crystallites mostly dissolved, as illustrated in the single image in Figure 5 (discharged). The dissolution starts from the upper right corner of the image during discharge, following the direction towards the center of the

current collector perforation and the cell center. The supplementary videos 1 and 2 provide more detail.

In subsequent cycles, dendritic beta sulfur forms, characterized by a more subtle, microcrystalline, branched or needle-like structure.[10,37] These are heavily obscured by the lithium dendrite phase contrast as seen in Figure 5 (charged). For illustrating the presence of beta-sulfur an image from the beginning of the second voltage plateau during charging, where the sulfur crystallites begin to form, has been selected. An image just at the onset of the second voltage plateau has been subtracted to remove the lithium dendrite pattern. The result (**Figure S7**) shows dark needle-like structure patterns of the sulfur crystallites. When the battery is discharged, lithium pitting corrosion is evident. During charging, shifting high-contrast areas

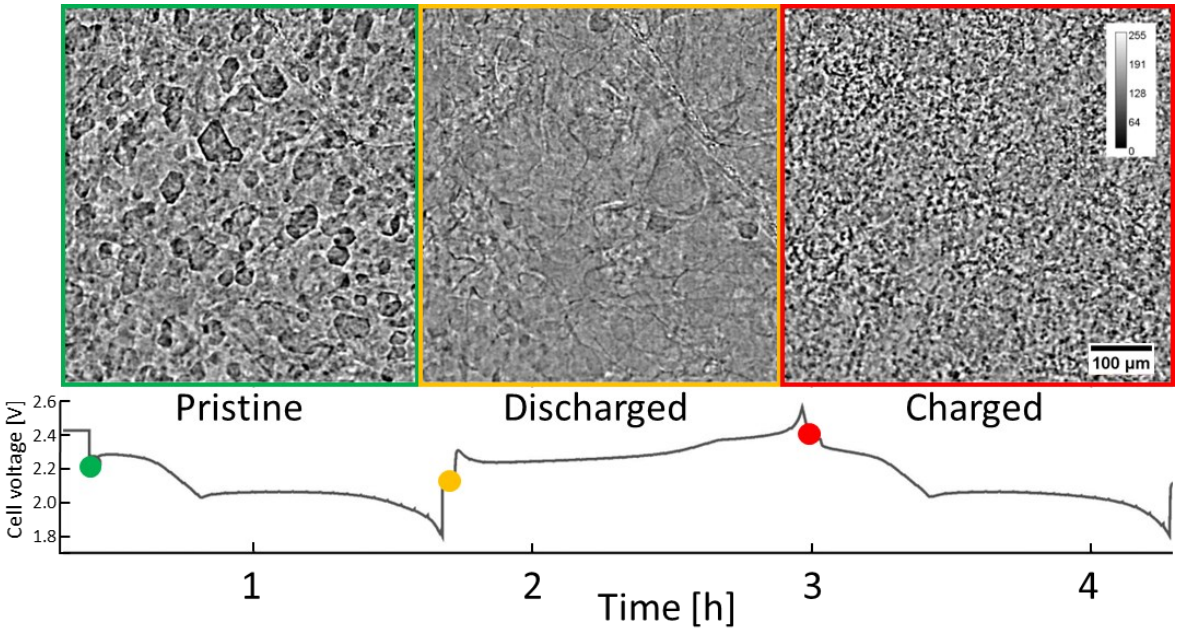

Figure 5: Phase contrast radiographies of cell Z2 at different states of charge. In the pristine state alpha sulfur crystals are clearly visible. In the discharged state, the sulfur crystals are dissolved, and the lithium surface is in the most stripped state. In the charged state, a high degree of phase contrast regions in the micrometer size is caused by the overlap of dendritic mossy lithium deposits and beta sulfur crystallites.

indicate the formation of mossy lithium. Tracking these changes is challenging due to overlapping regions across four lithium layers and variations in brightness. In the charged state, the delicate structures of lithium dendrites develop, with the contrasting sulfur crystallites barely distinguishable. Detailed examination of these patterns is available in SI videos 3 and 4. Synchrotron phase contrast radiography revealed two types of wetting effects. Gas layers that display breathing motions during charge and discharge cycles were identified at phase boundaries. The SI video 5 shows enhanced visualization of wetting lines and the edges of lithium pitting in the discharged state, using moving median enhancement and an edge-

enhancing filter. This treatment also highlights the distinct contrast of the mossy lithium phase when charged.

The radiography also captures wetting fronts throughout the cycling process, covering the entire image area. At least two distinct unobstructed gas/liquid phase boundaries were seen, likely located at flat surfaces such as the outer cell pack and between the separator and lithium anode. Directional reaction fronts were noted, particularly during the initial dissolution of sulfur crystallites, influenced by factors such as the cell's location (center, outer rim), position relative to internal components (perforations, tabs), and the shape of the cell pack (wrinkles, bends, excess electrolyte). These kinetic effects can be explored in SI video 1.

The standard deviation (SD) of radiography image pixel values serves as a simple approximate descriptor for the presence of particles or other features, applicable to both acquisition methods at BAMline and μCT (see section 2.5). **Figure 6** compares the standard deviation extracted from image pixel statistics from both imaging techniques and demonstrates the effect of median pseudo-flatfield normalization image-enhancing treatment, with color coding representing different cycle numbers from blue to red. The normalization by a static flatfield shows Li-dendrite phase contrast and overlaying sulfur crystallite growth for BAMline images, Figure 6A. Both processes contribute most toward the charged state. The contrast minimum in the discharged state reflects the state of least visible features by the phase contrast technique. The same method for μCT images shows the strong absorption of sulfur crystallites in the charged state, Figure 6B. The absorption of lithium sulfide deposits creates a lower and broader maximum in the discharged state. Apparent pitting of lithium may contribute to this as the electrolyte filled pits create pixel with higher attenuation.

The moving median pseudo flatfield enhancement (MovMedSD) emphasizes rapid changes and masks slow gradual changes. Thus, the pronounced phase boundaries of wetting domains visible in BAMline images for the discharged state give rise to a maximum of the standard deviation, Figure 6C. The μCT images become more sensitive as well and additional bright speckles of lithium dendrites contribute to the standard deviation at the transition between the voltage plateaus, Figure 6D.

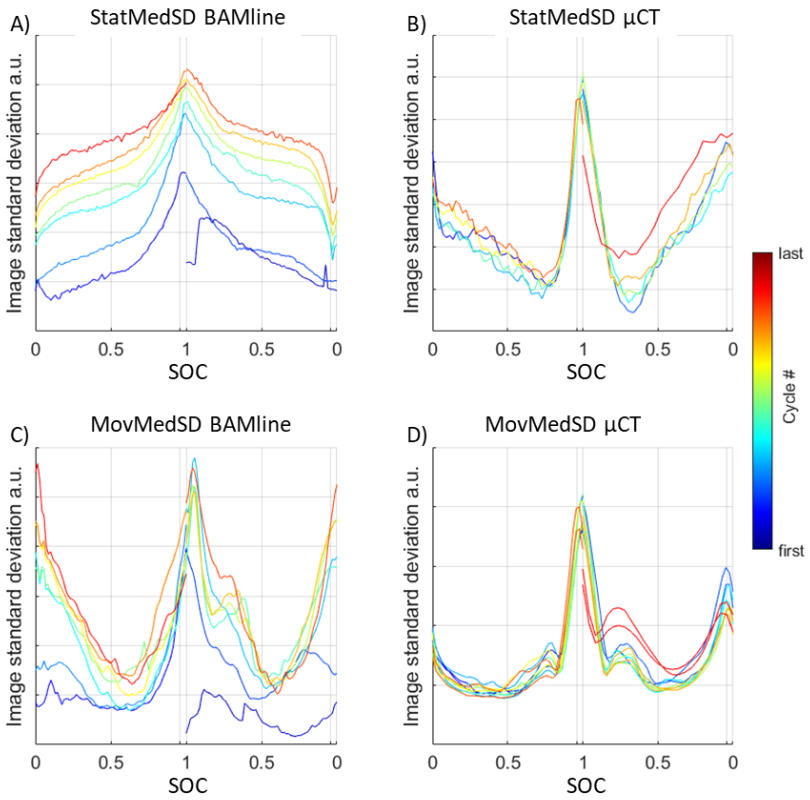

Figure 6: Radiography image pixel value standard deviation statistics depending on pseudo-flatfield normalization method. A) BAMline and B) µCT images normalized by a static flatfield. C) BAMline and D) µCT images standard deviation from moving median pseudo flatfield enhancement (MovMedSD).

2.5. Follow-up operando µCT radiography after the BAMline experiment.

The micro-computer tomography and radiography (µCT) is sensitive to absorption differences, which are governed by sulfur and lithium sulfide particles or accumulations, as well as lithium pitting corrosion. The µCT setup is described by Manke et al.[38]

The µCT electrochemistry (**Figure S2**) is very similar to the results obtained at the synchrotron and is described in the supporting information.

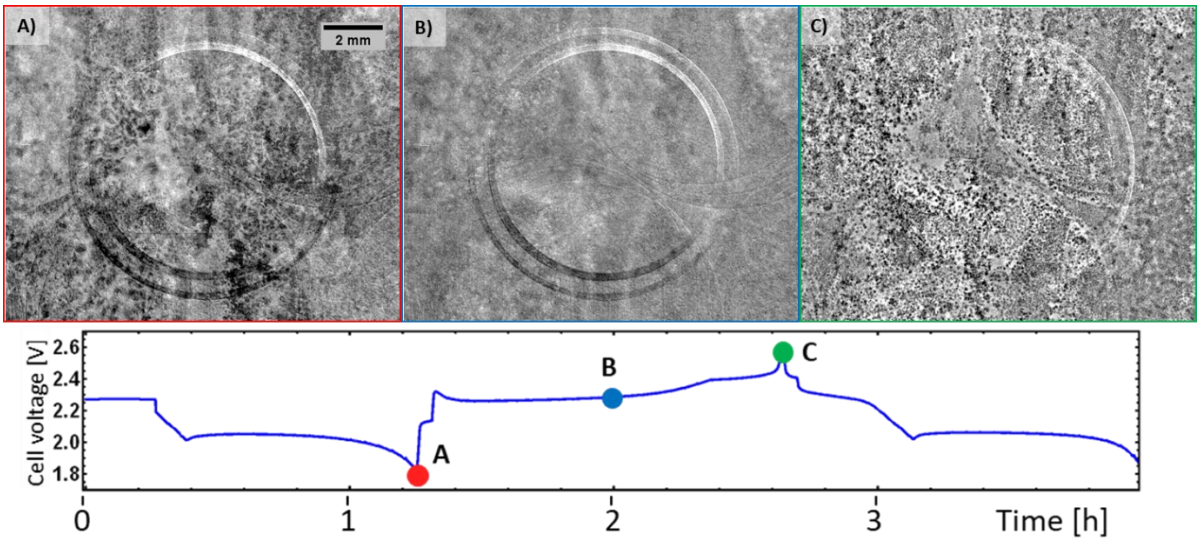

Figure 7 shows magnified radiographs of the pouch cell during cycling in the µCT setup, the full view images are in **Figure S1**. The material transformations behave as expected from the BAMline results. The sulfur species absorption is dominating the µCT contrast. Additional contribution comes from lithium pitting, which leads to increased attenuation due to an increase of the electrolyte volume in the X-ray beam path. See SI video 6 and video 7. A clear distinction between lithium pitting and Li_2S formation and accumulation cannot be drawn from the radiographies alone. The overlapping current collector perforations show no significant impact on the local cell behavior. The moving median enhancement of the images allows the detection of lithium depositions (best visible at the beginning of the high voltage plateau) and wetting lines (visible at the very beginning of the charge). See SI video 8.

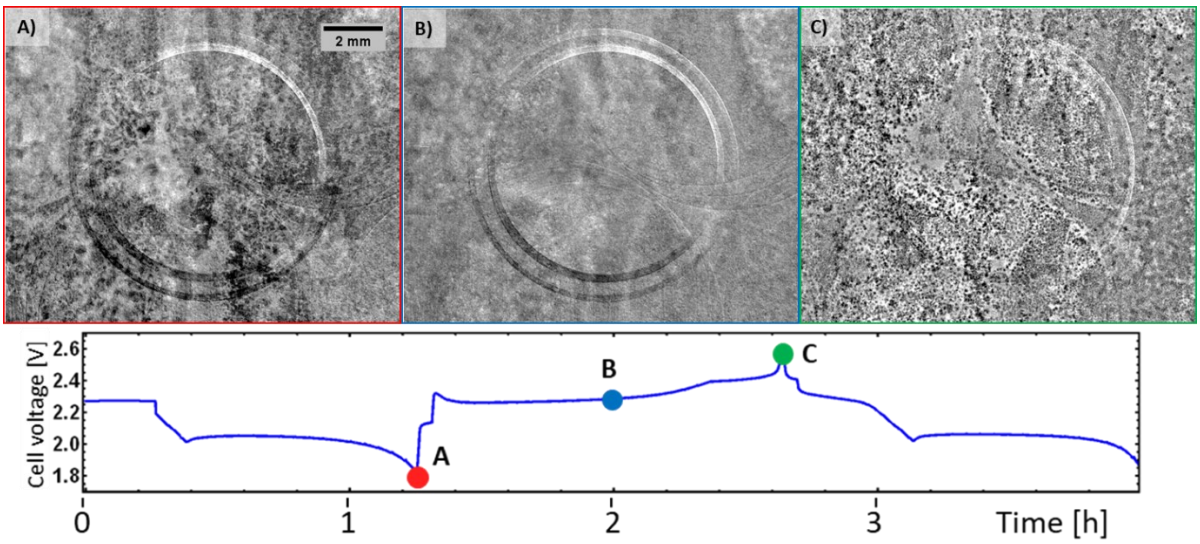

Figure 7: Radiographic images of the pouch cell during cycling in the µCT after experiments at the BAMline. A) discharged state B) half charged state C) charged state.

3. Conclusion

This study provides a comprehensive multimodal analysis of lithium-sulfur multilayer pouch cells, offering significant insights into their charge-discharge behavior and mechanistic processes. Our investigation of the cathode current collector perforation shows no significant systematic deviation in reaction behavior between current collector regions and perforation regions, indicating that local electrolyte volume distribution and electrode inhomogeneity predominantly influence material deposition kinetics and particle size.

Using synchrotron phase contrast radiography, we identified two distinct wetting effects characterized by dynamic phase boundaries, or "breathing motions," during charge and discharge cycles. Multiple gas/liquid phase boundaries, particularly at flat surfaces such as the outer cell pack and the separator-lithium interface, were observed. Notably, these boundaries do not hinder the cell's function. However, they indicate that electrolyte migration driven by internal volume changes could play an underestimated role in the practical operation of pouch cells. Additionally, directional reaction fronts during sulfur crystallite dissolution suggest a polysulfide-promoted mechanism.

The force measurements revealed variations up to 2.7 N, indicative of both reversible and irreversible processes. The observed irreversible pressure build-up is likely due to the accumulation of side products, while the reversible force behavior is governed by active material transformations dominated by lithium plating and stripping. The early sharp increase in force during charging suggests a pushing effect of lithium needles and loops, evolving into laterally growing mossy lithium as charging progresses.

Temperature evolution and electrolyte resistance are strongly correlated, primarily influenced by Joule heating, although polarization resistance significantly contributes to the temperature rise during the discharged state. The endothermic processes identified towards the end of the charge, which reverse at the beginning of discharge, hint at crystallization lattice enthalpy effects. These temperature and pressure observations are crucial for identifying potential safety issues during the early stages of cell development.

In summary, our findings not only enhance the understanding of lithium-sulfur pouch cell mechanisms but also underscore the importance of multimodal operando techniques in battery research. Future advances in operando tomography for intermediate-size pouch cells will facilitate a more detailed comprehension of complex electrode architectures and material distribution, aiding in designing optimized, high-performance energy storage solutions.

Videos in the supplementary information:

Video 1: BAM_Z2_main_StatMed_vs_MovMed

Video 2: BAM_Z2_low_StatMed

Video 3: BAM_Z2_main_zoom

Video 4: BAM_Z2_low_zoom

Video 5: BAM_Z2_main_MovMed_zoom_edgeenhance

Video 6: µCT_Z2_StatMed

Video 7: µCT_Z2_StatMed_zoom

Video 8: µCT_Z2_MovMed

Author Contributions

Author RM did the main experimental work, conceptualization, data analysis and draft writing, author SR did project planning, fundraising, supervision and mentoring, draft writing contribution and revision, author TB, SD, TA, HA, SK did cell manufacture and supplied experimental details, author HM and MS helped during synchrotron image acquisition and assisted in raw data analysis, authors NK, AH and IM supported the laboratory radiographic measurements and assisted in raw data analysis and data interpretation. S.R., S.K., S.D., H.A. and I.M. worked together on the fundraising and the development of conceptual ideas for the project. All authors took part in scientific discussions on the results.

4. Acknowledgment

We thank the German Federal Ministry of Education and Research (Bundesministerium für Bildung und Forschung) for funding the projects HiPoLiS (03XP0178B) and SkaLiS (03XP0398).

5. References

(1) Khan, F. M. N. U.; Rasul, M. G.; Sayem, A. S. M.; Mandal, N. K. Design and Optimization of Lithium-Ion Battery as an Efficient Energy Storage Device for Electric Vehicles: A Comprehensive Review. *J. Energy Storage* **2023**, *71*, 108033. https://doi.org/10.1016/j.est.2023.108033.

(2) Yao, W.; Xu, J.; Ma, L.; Lu, X.; Luo, D.; Qian, J.; Zhan, L.; Manke, I.; Yang, C.; Adelhelm, P.; Chen, R. Recent Progress for Concurrent Realization of Shuttle-Inhibition and Dendrite-Free Lithium–Sulfur Batteries. *Adv. Mater.* **2023**. https://doi.org/10.1002/ADMA.202212116.

(3) Cheng, X. B.; Yan, C.; Huang, J. Q.; Li, P.; Zhu, L.; Zhao, L.; Zhang, Y.; Zhu, W.; Yang, S. T.; Zhang, Q. The Gap between Long Lifespan Li-S Coin and Pouch Cells: The Importance of Lithium Metal Anode Protection. *Energy Storage Mater.* **2017**, *6*, 18–25. https://doi.org/10.1016/j.ensm.2016.09.003.

(4) Markötter, H.; Müller, B. R.; Kupsch, A.; Evsevleev, S.; Arlt, T.; Ulbricht, A.; Dayani, S.; Bruno, G. A Review of X-Ray Imaging at the BAM *Line* (BESSY II). *Adv. Eng. Mater.* **2023**, *25* (11). https://doi.org/10.1002/adem.202201034.

(5) Ziesche, R. F.; Arlt, T.; Finegan, D. P.; Heenan, T. M. M.; Tengattini, A.; Baum, D.; Kardjilov, N.; Markötter, H.; Manke, I.; Kockelmann, W.; Brett, D. J. L.; Shearing, P. R. 4D Imaging of Lithium-Batteries Using Correlative Neutron and X-Ray Tomography with a Virtual Unrolling Technique. *Nat. Commun.* **2020**, *11* (1), 1–11. https://doi.org/10.1038/s41467-019-13943-3.

(6) Risse, S.; Juhl, A.; Mascotto, S.; Arlt, T.; Markö, H.; Andréhilger, A.; Manke, I.; Frö, M. Detailed and Direct Observation of Sulfur Crystal Evolution During Operando Analysis of a Li−S Cell with Synchrotron Imaging. *J. Phys. Chem. Lett* **2020**, *11*, 5679. https://doi.org/10.1021/acs.jpclett.0c01284.

(7) Bradbury, R.; Dewald, G. F.; Kraft, M. A.; Arlt, T.; Kardjilov, N.; Janek, J.; Manke, I.; Zeier, W. G.; Ohno, S. Visualizing Reaction Fronts and Transport Limitations in Solid-State Li–S Batteries via Operando Neutron Imaging. *Adv. Energy Mater.* **2023**, *13* (17). https://doi.org/10.1002/aenm.202203426.

(8) Sadd, M.; Xiong, S.; Bowen, J. R.; Marone, F.; Matic, A. Investigating Microstructure Evolution of Lithium Metal during Plating and Stripping via Operando X-Ray Tomographic Microscopy. *Nat. Commun.* **2023**, *14* (1), 854. https://doi.org/10.1038/s41467-023-36568-z.

(9) Boenke, T.; Härtel, P.; Dörfler, S.; Abendroth, T.; Schwotzer, F.; Althues, H.; Kaskel, S. Sulfur Transfer Melt Infiltration for High-Power Carbon Nanotube Sheets in Lithium-Sulfur Pouch Cells. *Batter. Supercaps* **2021**, batt.202100033. https://doi.org/10.1002/batt.202100033.

(10) Müller, R.; Manke, I.; Hilger, A.; Kardjilov, N.; Boenke, T.; Reuter, F.; Dörfler, S.; Abendroth, T.; Härtel, P.; Althues, H.; Kaskel, S.; Risse, S. Operando Radiography and Multimodal Analysis of Lithium–Sulfur Pouch Cells—Electrolyte Dependent Morphology Evolution at the Cathode. *Adv. Energy Mater.* **2022**, *12* (13), 2103432. https://doi.org/10.1002/AENM.202103432.

(11) Schmidt, F.; Korzhenko, A.; Härtel, P.; Reuter, F. S.; Ehrling, S.; Dörfler, S.; Abendroth, T.; Althues, H.; Kaskel, S. Influence of External Stack Pressure on the Performance of Li-S Pouch Cell. *J. Phys. Energy* **2022**, *4* (1), 014004. https://doi.org/10.1088/2515-7655/ac4ee3.

(12) Rack, A.; Zabler, S.; Müller, B. R.; Riesemeier, H.; Weidemann, G.; Lange, A.; Goebbels, J.; Hentschel, M.; Görner, W. High Resolution Synchrotron-Based Radiography and Tomography Using Hard X-Rays at the BAMline (BESSY II). *Nucl. Instruments Methods Phys. Res. Sect. A Accel. Spectrometers, Detect. Assoc. Equip.* **2008**, *586* (2), 327–344. https://doi.org/10.1016/j.nima.2007.11.020.

(13) Wood, K. N.; Kazyak, E.; Chadwick, A. F.; Chen, K.-H.; Zhang, J.-G.; Thornton, K.; Dasgupta, N. P. Dendrites and Pits: Untangling the Complex Behavior of Lithium Metal Anodes through Operando Video Microscopy. *ACS Cent. Sci.* **2016**, *2* (11), 790–801. https://doi.org/10.1021/acscentsci.6b00260.

(14) Yu, S.-H.; Huang, X.; Schwarz, K.; Huang, R.; Arias, T. A.; Brock, J. D.; Abruña, H. D. Direct Visualization of Sulfur Cathodes: New Insights into Li–S Batteries via Operando X-Ray Based Methods. *Energy Environ. Sci.* **2018**, *11* (1), 202–210. https://doi.org/10.1039/C7EE02874A.

(15) Cheng, J.-H.; Assegie, A. A.; Huang, C.-J.; Lin, M.-H.; Tripathi, A. M.; Wang, C.-C.; Tang, M.-T.; Song, Y.-F.; Su, W.-N.; Hwang, B. J. Visualization of Lithium Plating and Stripping via in Operando Transmission X-Ray Microscopy. *J. Phys. Chem. C* **2017**, *121* (14), 7761–7766. https://doi.org/10.1021/acs.jpcc.7b01414.

(16) Wang, Y.; Dang, D.; Xiao, X.; Cheng, Y.-T. Structure and Mechanical Properties of Electroplated Mossy Lithium: Effects of Current Density and Electrolyte. *Energy Storage Mater.* **2020**, *26*, 276–282. https://doi.org/10.1016/j.ensm.2020.01.004.

(17) Charalambous, H.; Borkiewicz, O. J.; Colclasure, A. M.; Yang, Z.; Dunlop, A. R.; Trask, S. E.; Jansen, A. N.; Bloom, I. D.; Ruett, U.; Wiaderek, K. M.; Ren, Y. Comprehensive Insights into Nucleation, Autocatalytic Growth, and Stripping Efficiency for Lithium Plating in Full Cells. *ACS Energy Lett.* **2021**, *6* (10), 3725–3733. https://doi.org/10.1021/acsenergylett.1c01640.

(18) Jozwiuk, A.; Berkes, B. B.; Weiß, T.; Sommer, H.; Janek, J.; Brezesinski, T. The Critical Role of Lithium Nitrate in the Gas Evolution of Lithium–Sulfur Batteries. *Energy Environ. Sci.* **2016**, *9* (8), 2603–2608. https://doi.org/10.1039/C6EE00789A.

(19) Chen, X.; Hou, T.-Z.; Li, B.; Yan, C.; Zhu, L.; Guan, C.; Cheng, X.-B.; Peng, H.-J.; Huang, J.-Q.; Zhang, Q. Towards Stable Lithium-Sulfur Batteries: Mechanistic Insights into Electrolyte Decomposition on Lithium Metal Anode. *Energy Storage Mater.* **2017**, *8*, 194–201. https://doi.org/10.1016/j.ensm.2017.01.003.

(20) Schneider, H.; Weiß, T.; Scordilis-Kelley, C.; Maeyer, J.; Leitner, K.; Peng, H.-J.; Schmidt, R.; Tomforde, J. Electrolyte Decomposition and Gas Evolution in a Lithium-Sulfur Cell upon Long-Term Cycling. *Electrochim. Acta* **2017**, *243*, 26–32. https://doi.org/10.1016/j.electacta.2017.05.034.

(21) Waluś, S.; Offer, G.; Hunt, I.; Patel, Y.; Stockley, T.; Williams, J.; Purkayastha, R. Volumetric Expansion of Lithium-Sulfur Cell during Operation – Fundamental Insight into Applicable Characteristics. *Energy Storage Mater.* **2018**, *10*, 233–245. https://doi.org/10.1016/j.ensm.2017.05.017.

(22) Li, M.; Wang, Z.; Detsi, E. In Situ Electrochemical Dilatometry Study of (De)Lithiation and Polysulfide Dissolution-Induced Dimensional Changes in Lithium-Sulfur Cathodes during Charging and Discharging. *J. Electrochem. Soc.* **2020**, *167* (5), 050505. https://doi.org/10.1149/1945-7111/ab63c1.

(23) Diaz, M.; Kushima, A. Direct Observation and Quantitative Analysis of Lithium Dendrite Growth by In Situ Transmission Electron Microscopy. *J. Electrochem. Soc.* **2021**, *168* (2), 020535. https://doi.org/10.1149/1945-7111/abe5ec.

(24) Becherer, J.; Kramer, D.; Mönig, R. The Growth Mechanism of Lithium Dendrites and Its Coupling to Mechanical Stress. *J. Mater. Chem. A* **2022**, *10* (10), 5530–5539. https://doi.org/10.1039/D1TA10920K.

(25) Steiger, J.; Richter, G.; Wenk, M.; Kramer, D.; Mönig, R. Comparison of the Growth of Lithium Filaments and Dendrites under Different Conditions. *Electrochem. commun.* **2015**, *50*, 11–14. https://doi.org/10.1016/j.elecom.2014.11.002.

(26) Steiger, J.; Kramer, D.; Mönig, R. Mechanisms of Dendritic Growth Investigated by in Situ Light Microscopy during Electrodeposition and Dissolution of Lithium. *J. Power Sources* **2014**, *261*, 112–119. https://doi.org/10.1016/j.jpowsour.2014.03.029.

(27) Steiger, J.; Kramer, D.; Mönig, R. Microscopic Observations of the Formation, Growth and Shrinkage of Lithium Moss during Electrodeposition and Dissolution. *Electrochim. Acta* **2014**, *136*, 529–536. https://doi.org/10.1016/j.electacta.2014.05.120.

(28) Michael, H.; Jervis, R.; Brett, D. J. L.; Shearing, P. R. Developments in Dilatometry for Characterisation of Electrochemical Devices. *Batter. Supercaps* **2021**, *4* (9), 1378–1396. https://doi.org/10.1002/batt.202100027.

(29) Escher, I.; Hahn, M.; A. Ferrero, G.; Adelhelm, P. A Practical Guide for Using Electrochemical Dilatometry as Operando Tool in Battery and Supercapacitor Research. *Energy Technol.* **2022**, *10* (5). https://doi.org/10.1002/ente.202101120.

(30) Brieske, D. M.; Warnecke, A.; Sauer, D. U. Modeling the Volumetric Expansion of the Lithium-Sulfur Battery Considering Charge and Discharge Profiles. *Energy Storage Mater.* **2023**, *55*, 289–300. https://doi.org/10.1016/j.ensm.2022.11.053.

(31) Shahjalal, M.; Tripathy, Y.; Sheikh, M. Investigation on Thermal Performance Analysis of a Pouch Li-Ion Battery under Various Drive Cycle Profiles. *J. Energy Storage* **2023**, *73*, 108977. https://doi.org/10.1016/j.est.2023.108977.

(32) Stroe, D. I.; Knap, V.; Swierczynski, M.; Schaltz, E. Thermal Behavior and Heat Generation Modeling of Lithium Sulfur Batteries. *ECS Trans.* **2017**, *77* (11), 467–476. https://doi.org/10.1149/07711.0467ecst.

(33) Barchasz, C.; Boutafa, L.; Mayousse, E.; Chavillon, B. Diagnostic of Failure Mechanisms in Li/S Rechargeable Batteries Using Thermal Micro-Calorimetry Technique Applied to Pouch and Cylindrical Type Cells. *Electrochim. Acta* **2018**, *292*, 974–981. https://doi.org/10.1016/j.electacta.2018.09.167.

(34) Zhang, T.; Marinescu, M.; O'Neill, L.; Wild, M.; Offer, G. Modeling the Voltage Loss Mechanisms in Lithium–Sulfur Cells: The Importance of Electrolyte Resistance and Precipitation Kinetics. *Phys. Chem. Chem. Phys.* **2015**, *17* (35), 22581–22586.

https://doi.org/10.1039/C5CP03566J.

(35) Soni, R.; Robinson, J. B.; Shearing, P. R.; Brett, D. J. L.; Rettie, A.; Miller, T. S. Lithium-Sulfur Battery Diagnostics Through Distribution of Relaxation Times Analysis. *SSRN Electron. J.* **2022**. https://doi.org/10.2139/ssrn.4030055.

(36) Wang, S.; Huang, F.; Li, X.; Li, W.; Chen, Y.; Tang, X.; Jiao, S.; Cao, R. Regulating Li 2 S Deposition by Ostwald Ripening in Lithium–Sulfur Batteries. *ACS Appl. Mater. Interfaces* **2022**, *14* (3), 4204–4210. https://doi.org/10.1021/acsami.1c22025.

(37) Villevieille, C.; Novák, P. A Metastable β-Sulfur Phase Stabilized at Room Temperature during Cycling of High Efficiency Carbon Fibre–Sulfur Composites for Li–S Batteries. *J. Mater. Chem. A* **2013**, *1* (42), 13089. https://doi.org/10.1039/c3ta13072j.

(38) Kardjilov, N.; Hilger, A.; Manke, I. CONRAD-2: Cold Neutron Tomography and Radiography at BER II (V7). *J. large-scale Res. Facil. JLSRF* **2016**, *2*, A98. https://doi.org/10.17815/jlsrf-2-108.

Supporting Information

Multimodal *Operando* Analysis of Lithium Sulfur Multilayer Pouch Cells: An In-depth Investigation on Cell Component Design and Performance

Rafael Müller[a]*, Tom Boenke[b,c], Susanne Dörfler[b], Thomas Abendroth[b], Paul Härtel[b], Holger Althues[b], Stefan Kaskel[b,c], Nikolay Kardjilov[a], Henning Markötter[d], Michael Sintschuk[d], André Hilger[a], Ingo Manke[a], Sebastian Risse[a]*

[a] Institute for Electrochemical Energy Storage, Helmholtz-Zentrum Berlin, Hahn Meitner Platz 1, 14109 Berlin, Germany

[b] Fraunhofer IWS, Winterbergstraße 28, 01277 Dresden, Germany

[c] Technische Universität Dresden, Inorganic Chemistry I, Bergstr. 66, 01069 Dresden, Germany

[d] Bundesanstalt für Materialforschung und -Prüfung, 12205 Berlin, Germany

* Corresponding Authors: rafael.mueller@helmholtz-berlin.de & sebastian.risse@helmholtz-berlin.de

5.1. Pouch cell details

Table 1. Details of the cathode parameters for the investigated pouch cell.

Cell	Cathodes double sided #	Cathode Thickness + Al [µm]	Cathode Thickness no Al [µm]	Loading Density [g/cm³]	Sulfur content [%]	Sulfur loading [mg/cm²]	Sulfur mass [mg]	Cell capacity [mAh]
	3x ds	93	73	0.63	53.87	1.24	242.96	406.23

Table 2. Pouch cell parameters and first discharge conditions.

Cell	Electrolyte volume (V)	Electrolyte/Sulfur (E/S) ratio	Areal capacity C_A = C / A	1. Discharge C-rate	1. Discharge capacity	1. Discharge Sulfur utilization
Unit	µL	mL / g(S)	mAh/cm²	1/h	mAh/g	%
	1140	4.69	12.44	0.50	1058	63

Table 3. Absolute capacity values

Half cycle #	1	2	3	4	5	6	7	8	9	10	11	12	13	14
C [mAh]	256.60	252.20	252.96	258.79	260.46	261.35	263.30	264.88	263.08	266.31	263.85	267.10	263.37	266.91

5.2. Force sensor reading conversion

Calibrated SingleTact force sensor reading conversion: 0.5-1.5 V = 0-4.5 N

$$\boldsymbol{Load}\ (\boldsymbol{N}) = (\boldsymbol{Analog\ Output}\ (\boldsymbol{V}) - \boldsymbol{Baseline\ Output}(\boldsymbol{V}))\ /\mathbf{1}\ (\boldsymbol{V}) * \boldsymbol{Sensor\ Rating}\ (\boldsymbol{N})$$

A(sensor) = 1.767 cm²; A(electrode) = 32.66 cm²

p(sensor) = F / A(sensor) = x N / 1.767 cm²

p(pouch) = F / A(electrode) = x N / 32.66 cm²

1 N / cm² = 10 kPa

For x = 4 N → p(sensor) = 22.64 kPa; p(pouch) = 1.22 kPa

5.3. Results overview of the µCT experiment

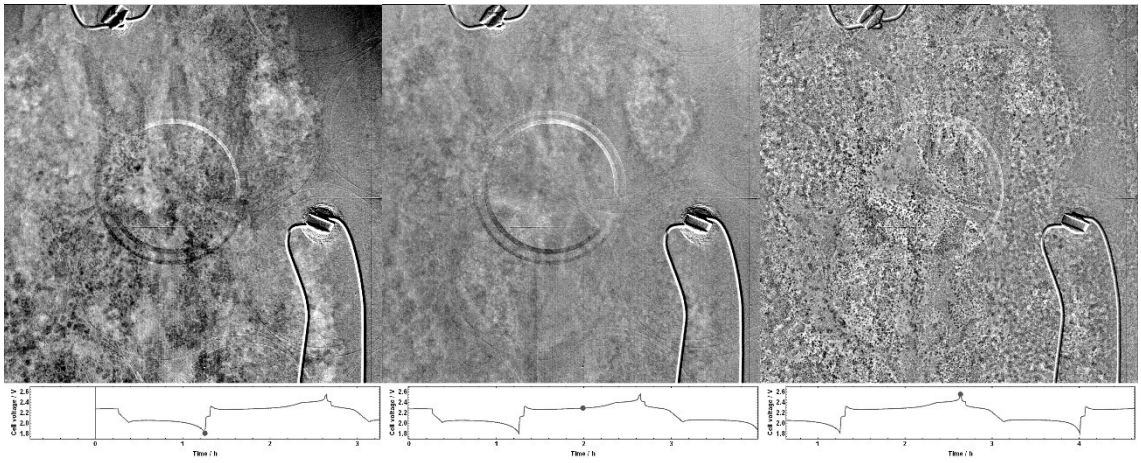

Figure S1: Full view µCT images in discharged, half charged, and fully charged state.

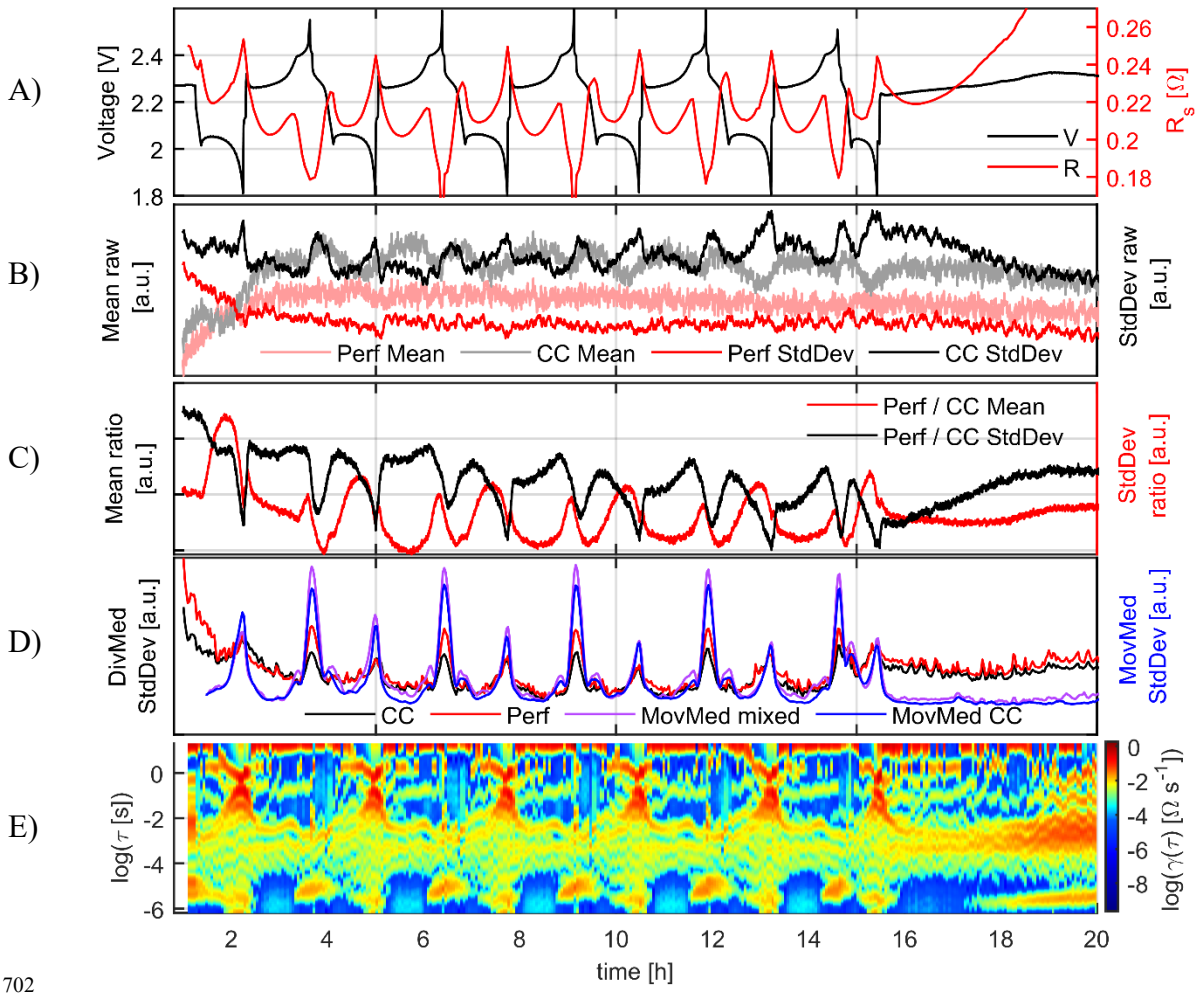

Figure S2: Operando cell µCT experiment after experiments at BAMline. Electrochemistry and radiography image statistics analysis. A) and E) Results from electrochemical charge-discharge measurement and operando EIS fitting: Voltage, solution resistance and DRT. B): Raw images standard deviation and mean of current collector (CC) and perforation (Perf) regions. C): Ratios of the CC region divided by the Perf region values reduce the

resulting value fluctuation and indicate some difference, but the relative magnitude is below 1% and less than a comparison of two different regions that cover both CC and perforation regions. D): Image standard deviations after image enhancing treatment by division by the median of all images (StatMed) and by division by a moving median of 31 images (MovMed), which suppresses the impact of slow changes and field-of-view drift. The similarity of CC and Perf regions is clearly visible from the StatMed plots. The standard deviation of the MovMed enhanced images shows plots that improve the visibility of changes at the beginning and end of the high-voltage plateaus. These can be attributed to the onset of sulphur deposition and the full dissolution of the sulphur deposits.

5.4. Image treatment methods

The moving median normalization appears to lessen the impact of image illumination gradients, as these are reduced by the resulting temporal and local median pseudo flatfield correction. The temporally localized changes of morphologic features on the radiographs (including particle deposition, wetting fronts and pitting corrosion edges) were extracted as one indicator value, the MovMedSD. This was derived by normalizing each radiograph by a moving median pseudo-flatfield of 31 images. The resulting curve illustrates rapid changes within one charge/discharge cycle while slow changes over several cycles are filtered out. Those slow processes encompass cell position drift, gradual electrolyte migration and decomposition, corrosion, and shift of static domains. The maxima after the charged state indicate the fastest change of image contrast happens when the sulfur particles start dissolving. A shoulder after the polysulfide discharge dip is growing with each cycle and might be related to wetting edges due to electrolyte redistribution. A maximum around the discharged state is growing likewise with cycle number. Visual inspection of the radiography videos suggests an increase of lithium pitting corrosion or related localized lithium sulfide deposition.

Li_2S is not visible as resolved species or contrast edges in phase contrast images, as the particle size is in the range below 1 µm due to the very low solubility. The Li_2S deposition may have an influence on the phase contrast images in an expectedly subtle and blurry fashion, as unresolved absorption and scattering may give a smeared-out contribution. In the µCT images a contribution can be discerned, when agglomerations are formed, as the materials attenuation has a larger impact on the image with this method. As an example, the attenuation of the current collector foils can be compared for both techniques. For 1, 2 and 3 overlaying layers of current collector foil, the attenuation in µCT images increases by 0.45 %, 0.81 % and 1.24 %, which is visible in radiography images. In phase contrast images, the values obtained are -0.05 %, -0.02 %, and -0.03 %, which is well below the count's standard deviation of 1.05 % and thus no attenuation contribution of the current collector foils is visible and contribution of Li_2S would be even lower.

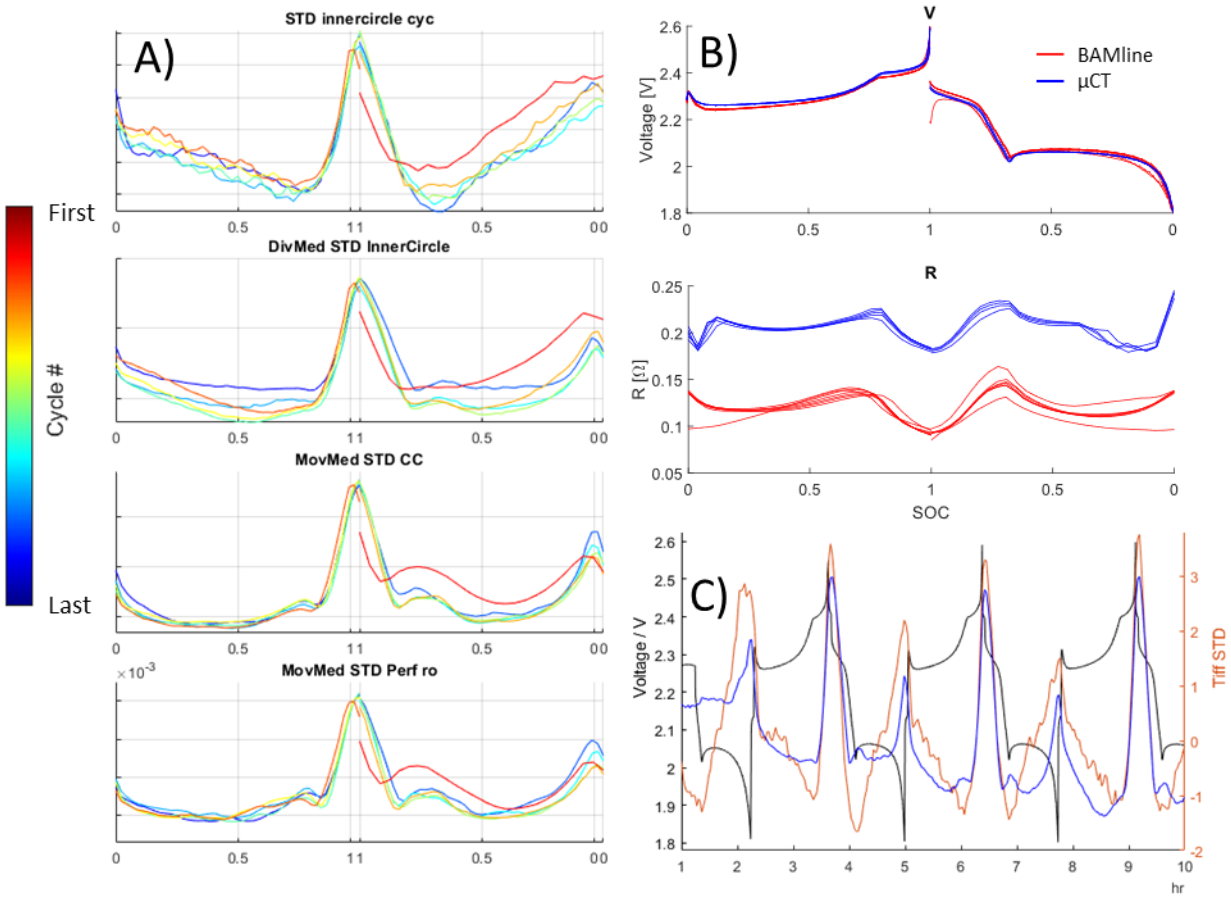

Figure S3: A) Operando cell µCT experiment image statistics normalized by SoC. First row SD from raw images. Second row from StatMedSD images. The moving median image treatment reduces noise and enhances fast changes and masks slow image changes. The rows 3 and 4 show CC and perforation region results for comparison. The difference appears negligible. B) Overlay of the voltage and resistance plots of the operando cell experiments at the BAMline (red) and at the µCT (blue). C) First 10 hours of the voltage curve of the operando cell at the µCT with a comparison of the image pixel standard deviation of two different image data treatment methods (orange: static median image normalization, blue: moving median normalization).

5.5. Discussion of the impact of the current collector perforation pattern:

Selected image area current collector (CC) versus perforation (Perf) pixel statistics were compared to test for possible differences of material transformation processes. The region-of-interest mask is shown in

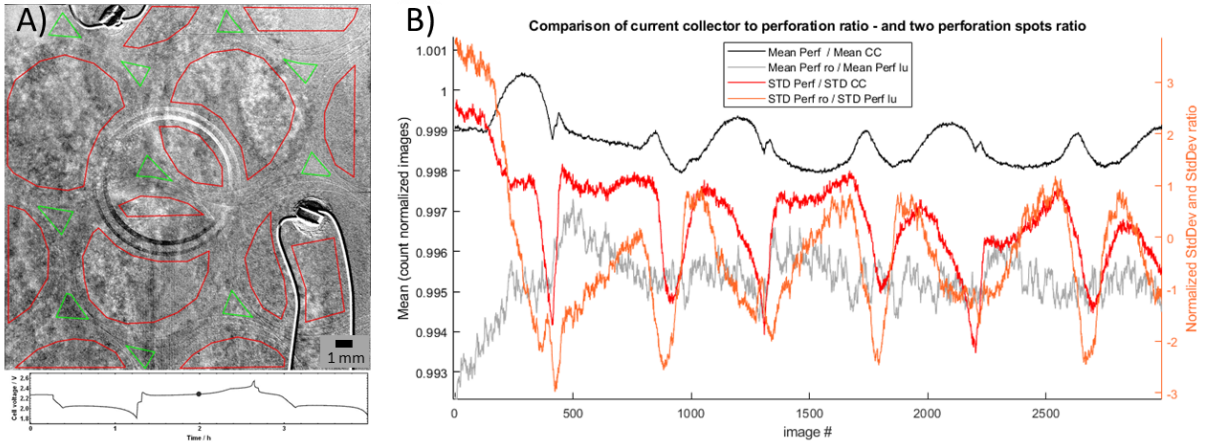

Figure S4.

The untreated data mean and standard deviation alone are too noisy and susceptible to beam intensity fluctuations and field-of-view drifts and yield ambiguous results see **Figure S2 B**. The treated data provide slight periodic behavior expressed at CC regions and division of perforation area by current collector area values appears to reduce fluctuations, see **Figure S2 C** and **D**. Nevertheless, similar behavior in the same order of magnitude is seen when different perforation regions of the current collector (

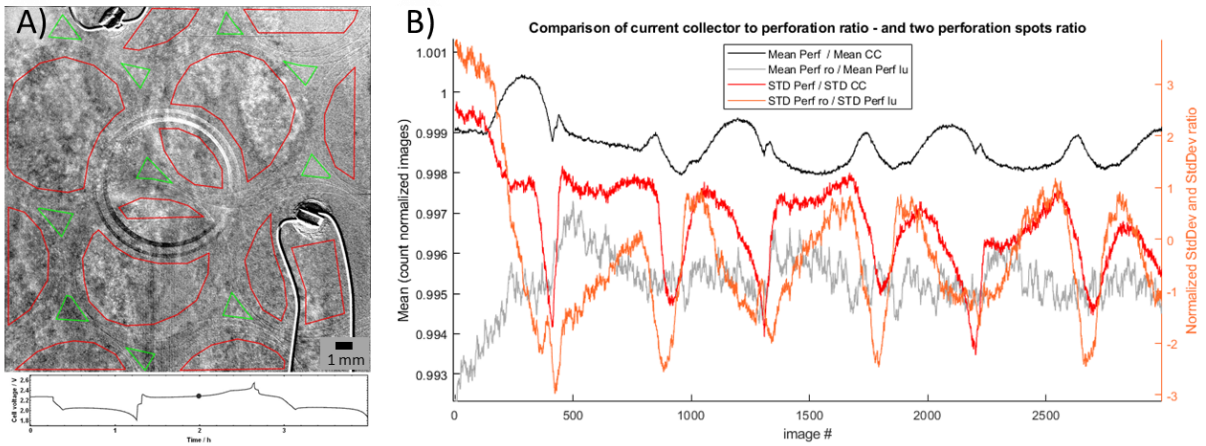

766 **Figure S4,**

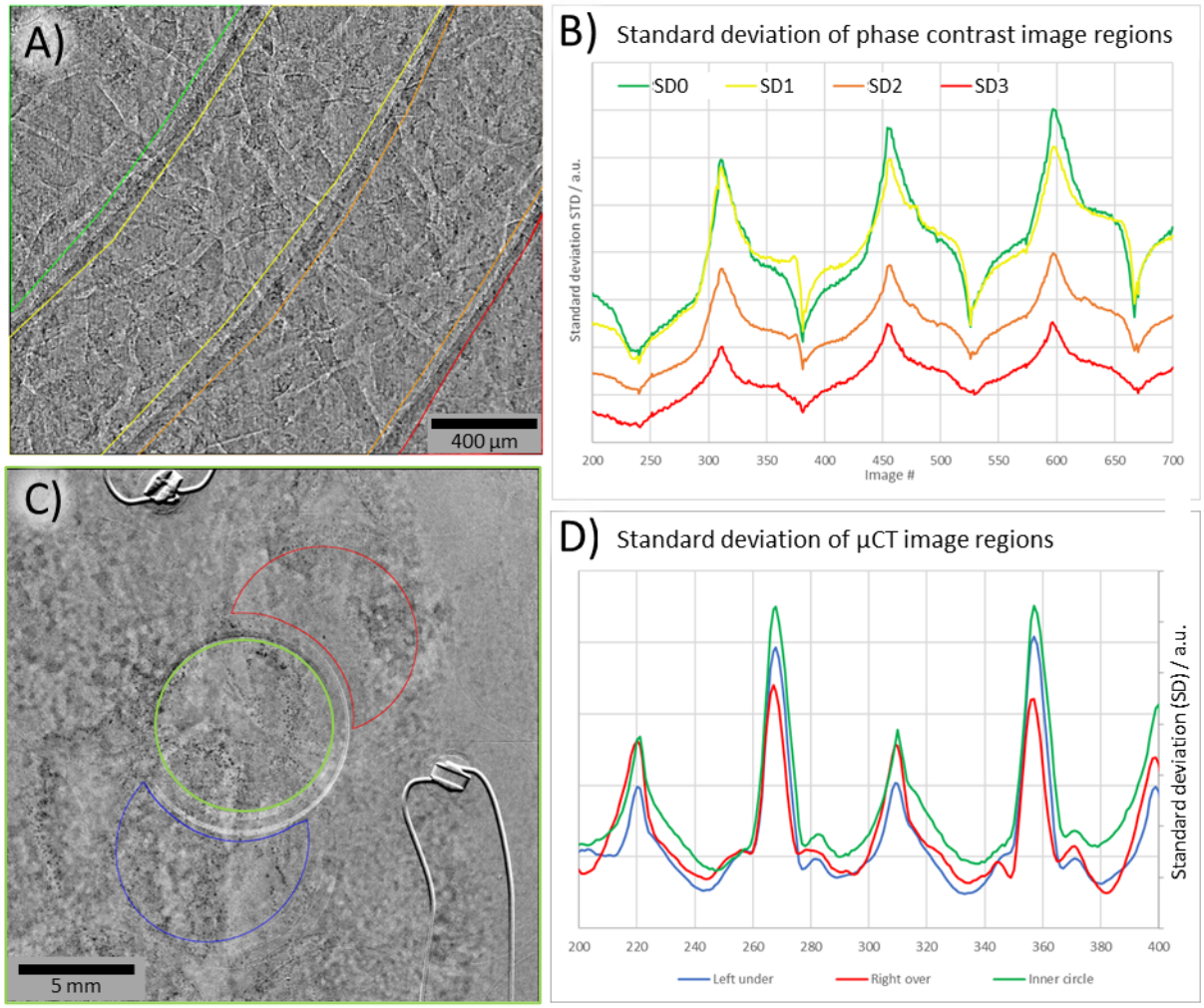

767

768 **Figure S5 C)** are compared.

769 This suggests that the temporal difference in particle formation kinetics is mainly related to

770 inhomogeneous local materials distribution and not to the pattern of the current collector.

771

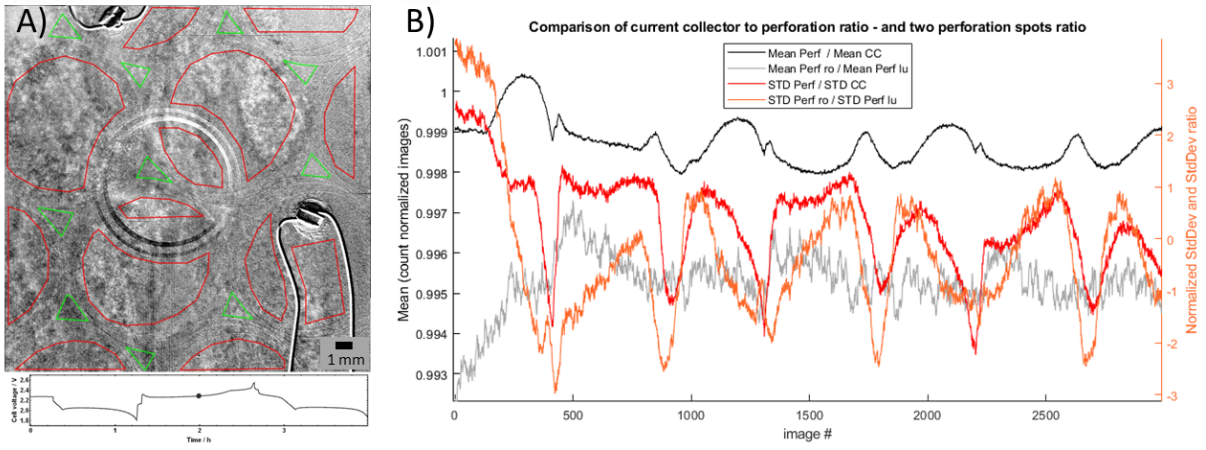

772

Figure S4: µCT radiography image with the regions of interest mask for current collector (green) and perforation areas (red). Comparison of two perforation spots' (lu = left under in blue and ro = right over in red in

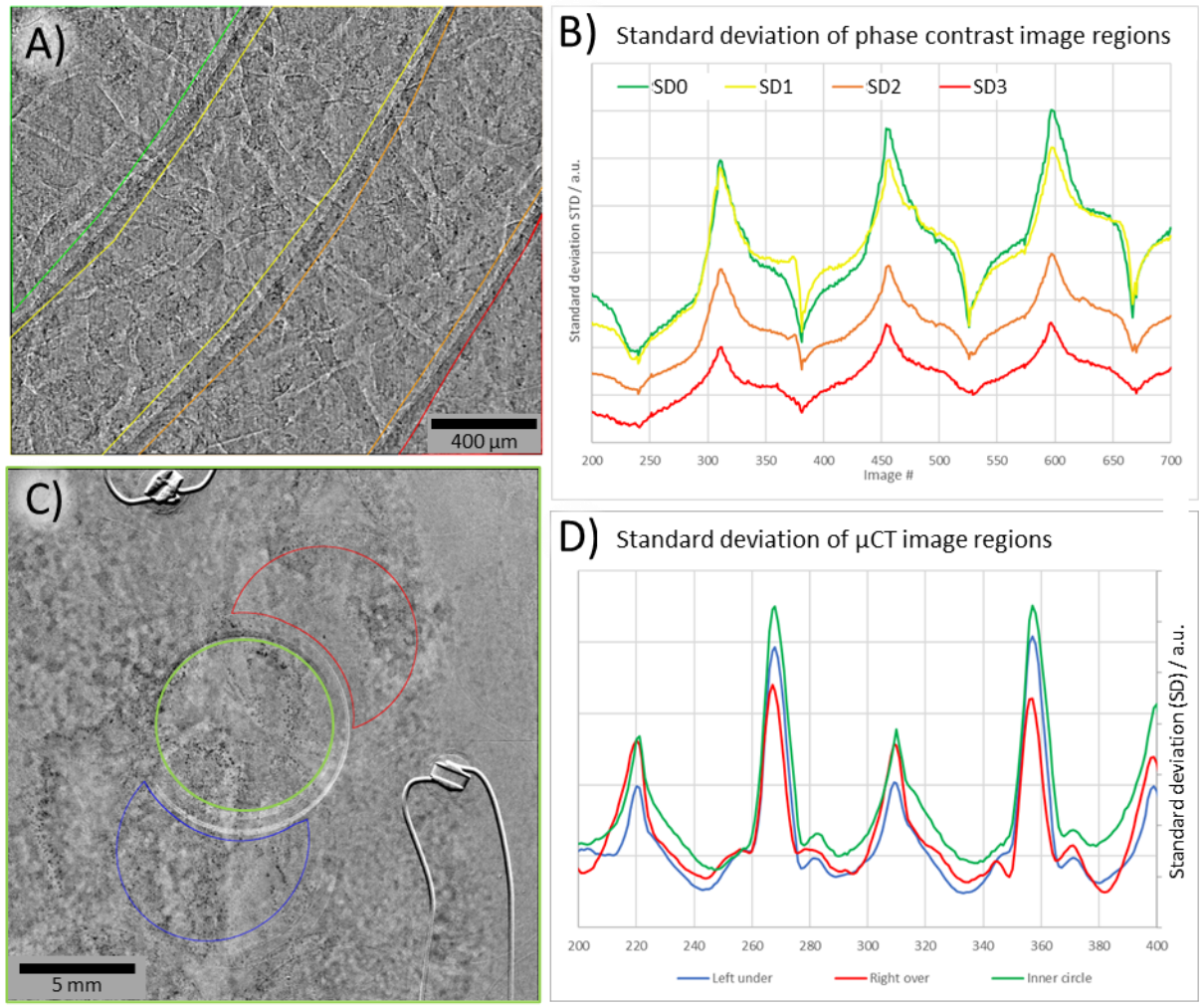

Figure S5 C) standard deviation and mean ratios to distinguish causality of current collector influence versus uncorrelated local differences. The ratio of the ro-spot to the lu-spot and the ratio of the ro-spot to the spot with

current collectors (green in

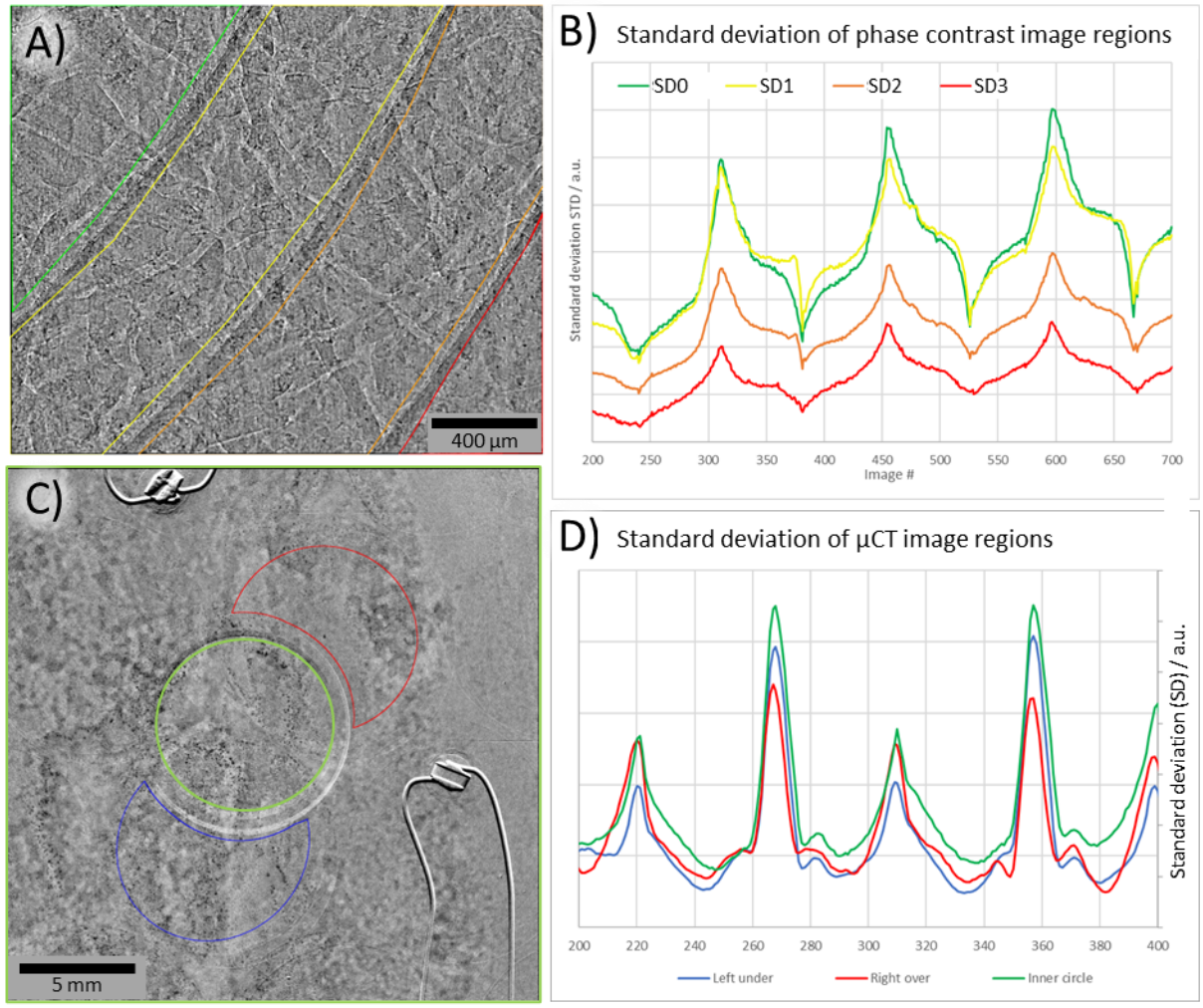

Figure S5 C) similar patterns for the SD. For the ratios of the mean values, a difference is observed but it is of a very low magnitude of +/- 0.1 %.

µCT perforation and CC comparison

The local counts and standard deviations are very sensitive to fluctuations in source intensity and illumination gradients. The fluctuations can be compensated by division of different regions, but the illumination gradient influence is thereby enhanced and creates an apparently systematic correlation. Here current collector and perforation domains suggest such a systematic correlation. This may be misleading, which can be shown by comparing two different perforation regions. A similar apparent systematic difference of mean or standard deviation ratio is observed.

Selected region discussion:

BAMline & µCT images have been segmented manually to separate region of interest (ROI) selections for pixel value statistics comparison for the current collector perforation layout. At

the BAMline the high magnification image can be split in the perforated region (top right) and three layers of current collector towards the bottom left (

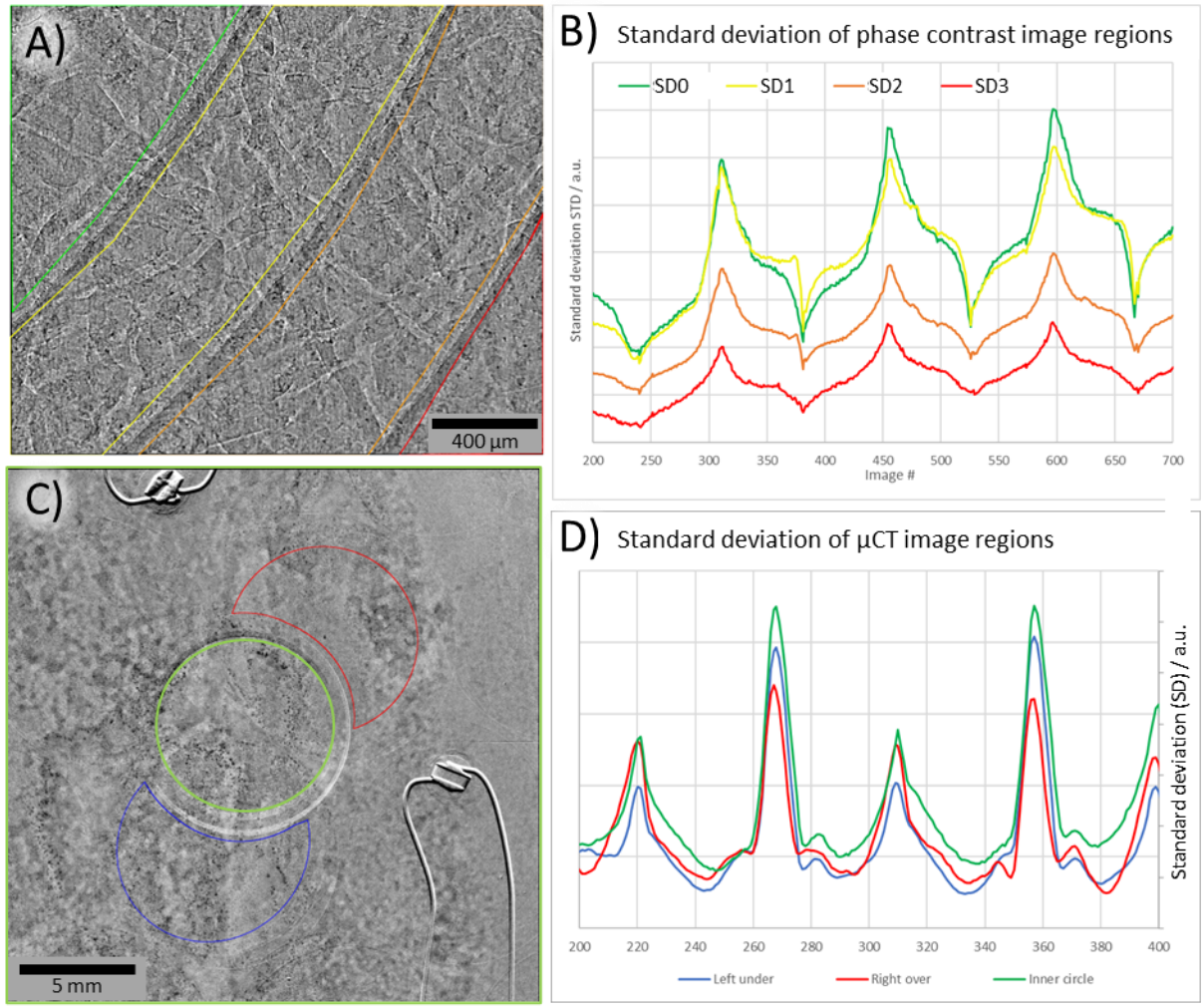

Figure S5 A). For the less magnified µCT images (

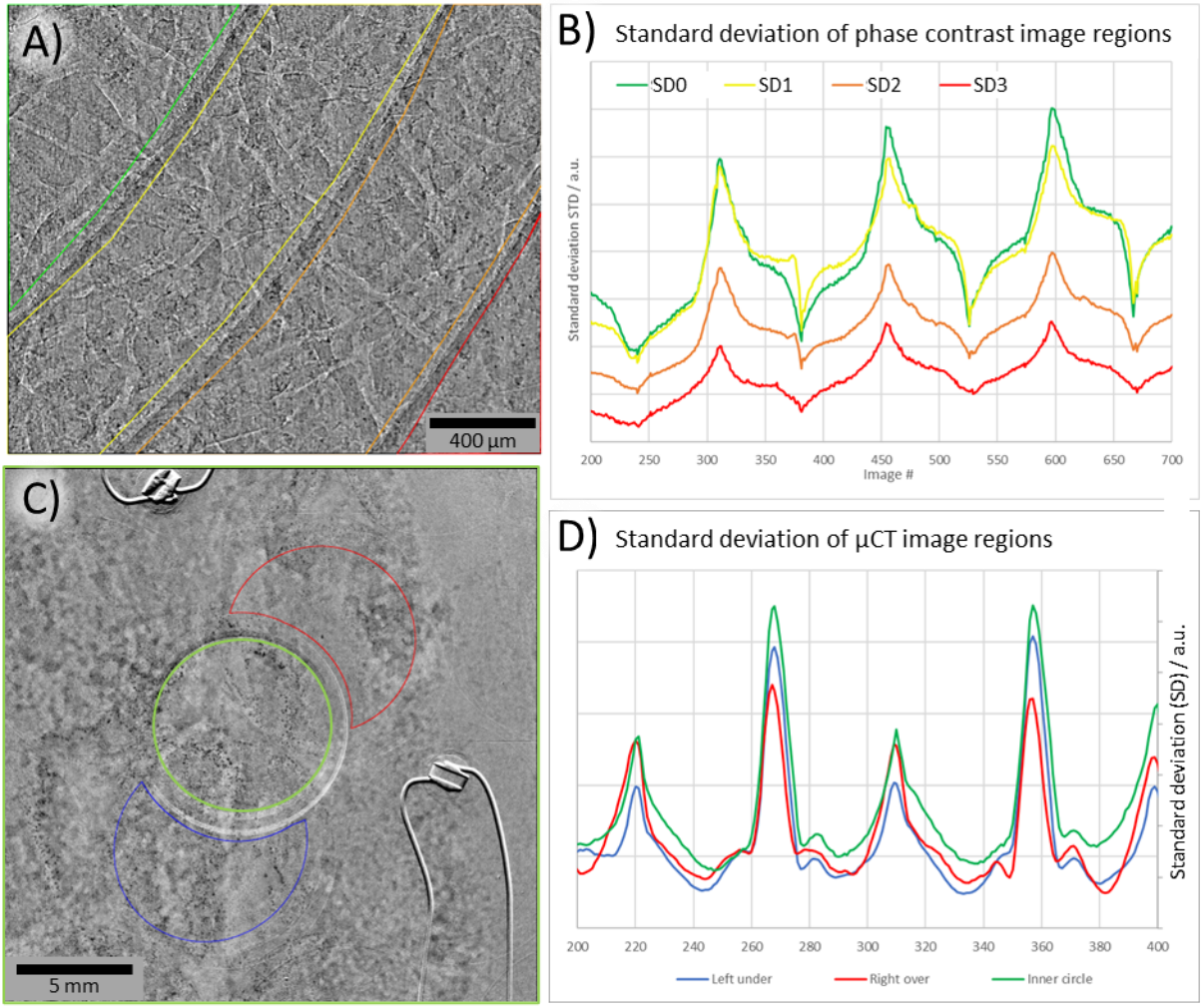

Figure S5 C) perforation holes are labelled in red. Green triangular shapes map the regions of overlapping current collector foil sheets. The inner circular drilled window is shown in orange. Artifact susceptible regions (outer and inner edges, drilling of holder window, cables, sensors, dead detector pixels) have generously been excluded.

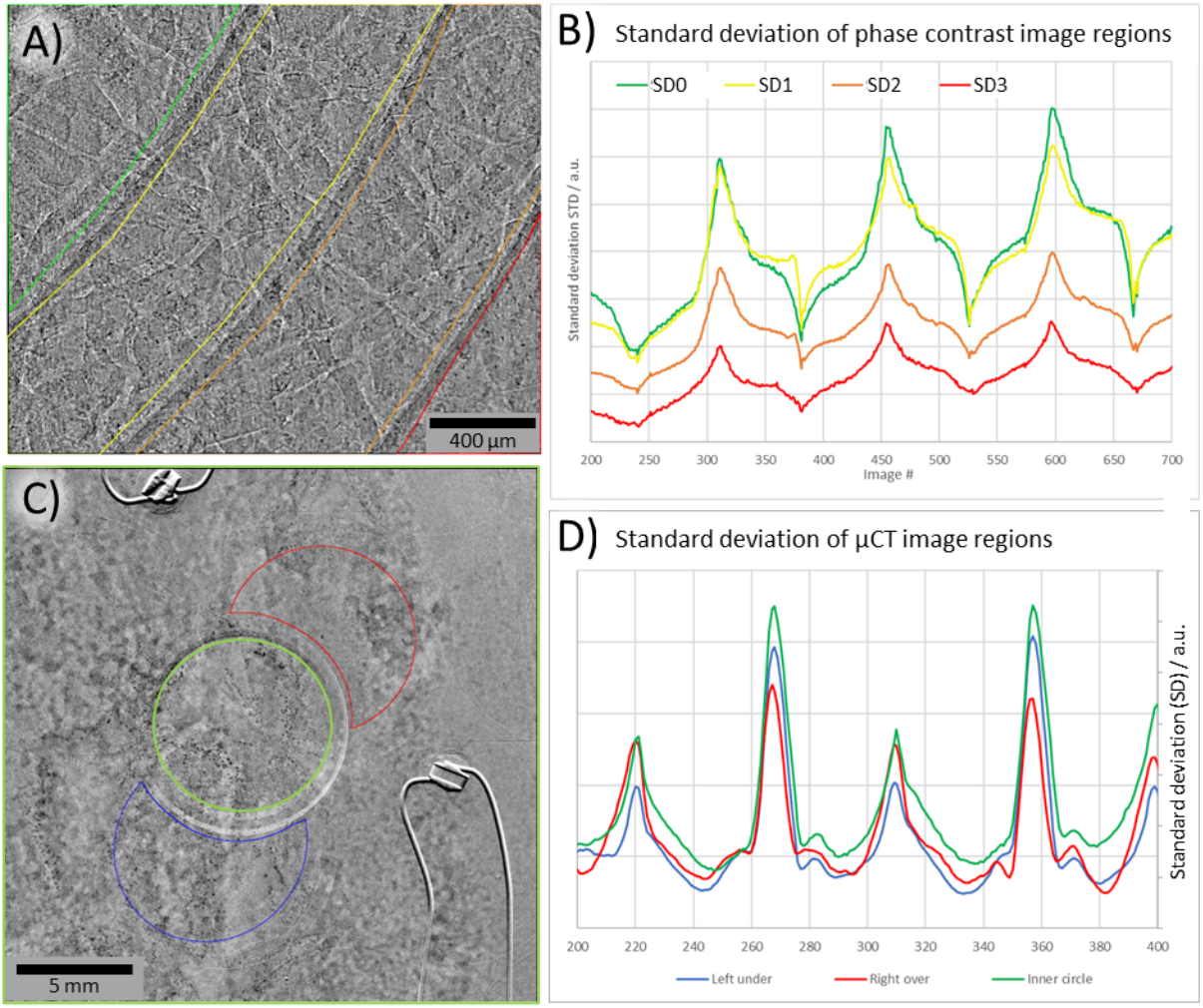

Figure S5: A) and B) Regions of interest on the phase contrast radiographies with 0 to 3 layers of current collector. The behavior of the regions standard deviation is qualitatively the same. C) and D) Comparison of different spots of the µCT measurement with and without current collector. No systematic discrepancies are detectable.

We compared two perforated spots, one right over (ro) and one to the left under (lu) the drilled hole in the holder. The particle formation kinetics are indicated by the pixel value SD and appear not to depend on the current collector. The qualitative similarity of the SD ratio curves of perforation/cc and perforation ro/lu does not suggest different precipitation kinetics at cc regions versus cc-free regions (

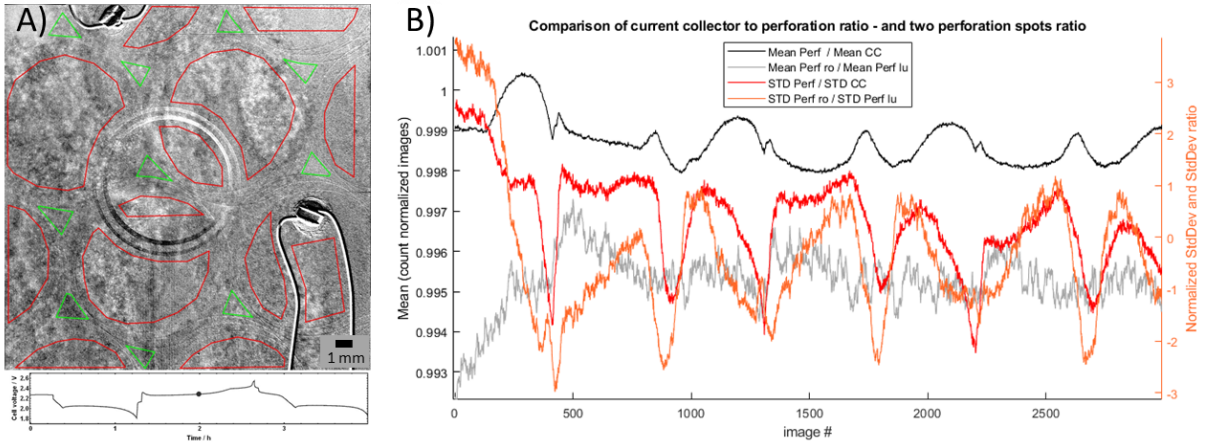

816

817 **Figure S4**). Local cell differences (like thickness, illumination, electrode morphology) appear to
818 dominate the residual deviations. In the SI videos visual temporal systematic differences are
819 also only observed locally and are not representative for the full cell area.

820

5.6. Multimodal results versus SoC

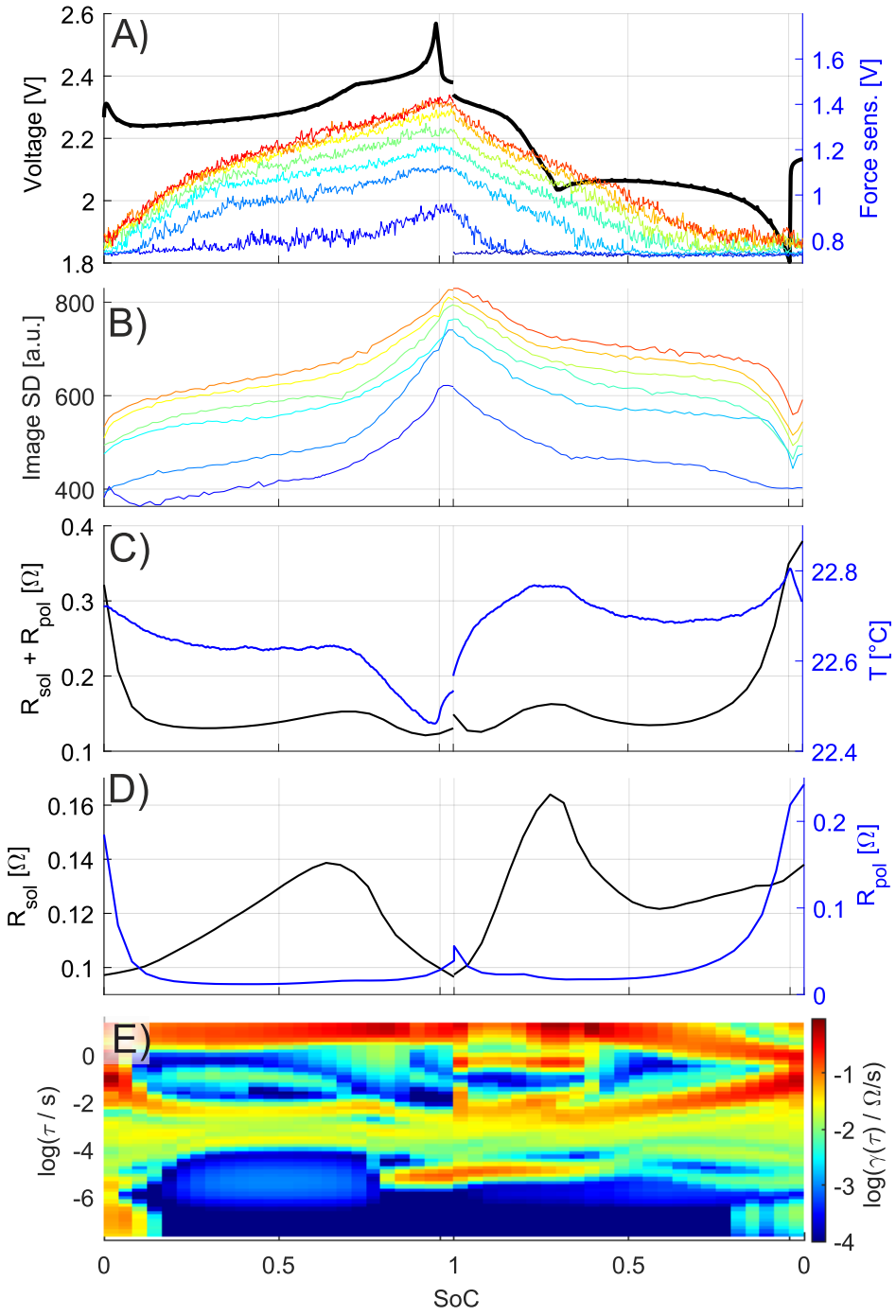

Figure S6: Multimodal results versus state of charge (SoC) of the BAMline measurement. The SoC axes include the potentiostatic OCP EIS measurements at the end of each charge/discharge segment. A) Averaged voltage curve. B) Radiography image SD from the second cycle. C) Left: Averaged sum of resistances. Right: Averaged temperature. D) Left: Averaged solution resistance. Right: Averaged polarization resistance calculated from DRT integration. E) Distribution of relaxation times.

Since the curves of voltage, temperature, and resistances are highly reproducible for the last six cycles, these results can be averaged and plotted versus state of charge for qualitative analysis

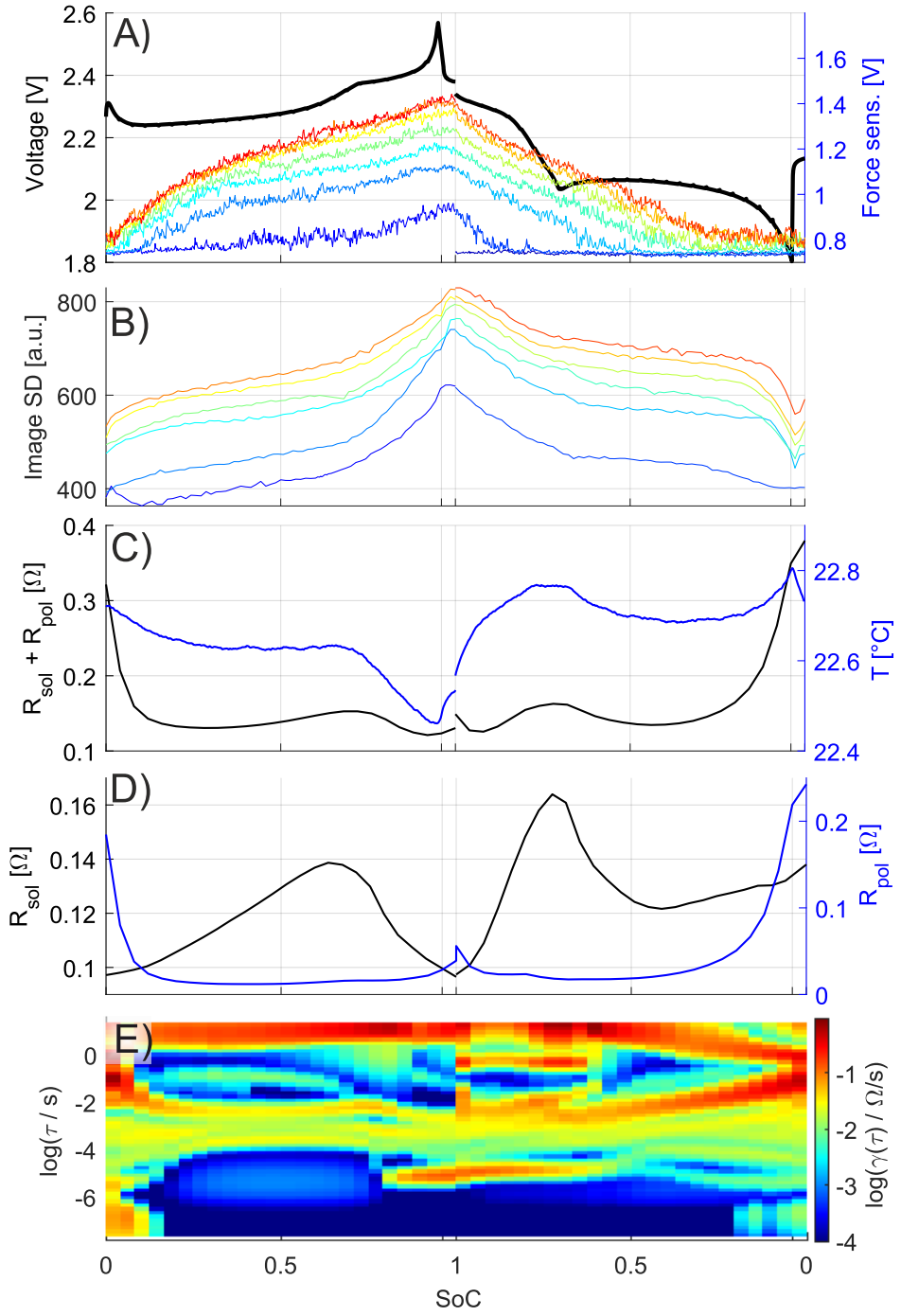

(**Figure S6**). This approach enhances feature visibility and allows a more detailed correlation.

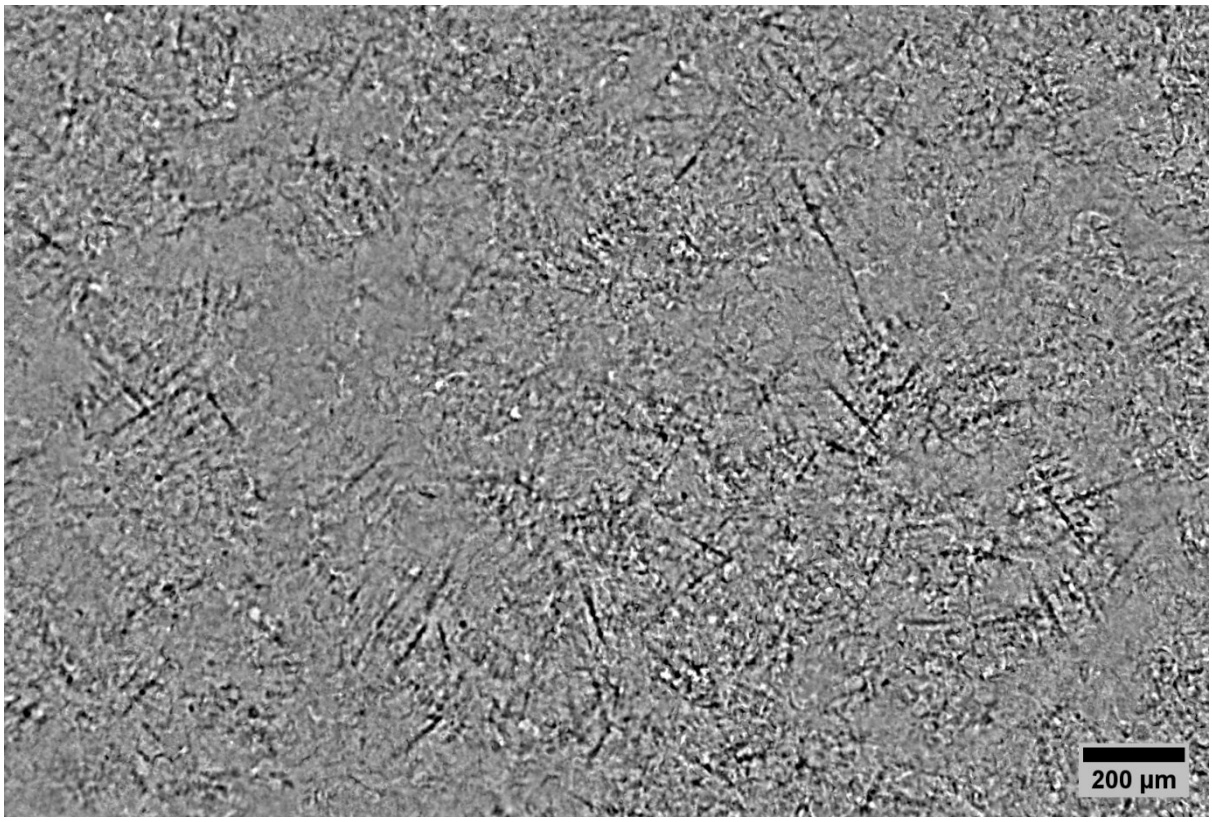

Figure S7: Section of a synchrotron radiography image at the second voltage plateau. The sulfur crystallite visibility was enhanced by subtraction of an image just at the onset of the second voltage plateau. Due to the similar state of charge, the pattern of the lithium dendrites is selectively suppressed by the subtraction leaving an improved visibility of the superimposed sulfur needle structures.

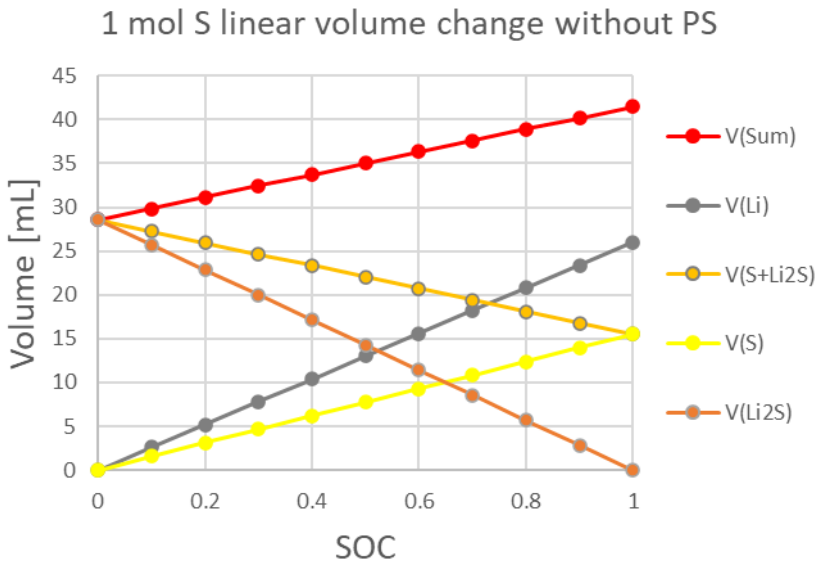

Figure S8: Plot showing an example calculation for the solid species volumes contributions. Equivalents based on 1 mol sulfur have been interpolated linearly to guide the eye, but it is not reflecting the true presence of intermediate material states for liquid electrolyte systems. Nevertheless, the final lithium volume contribution with 26 mL is larger than the combined sulfur/sulfide contribution (28.56 - 16.36 = 12.2 mL).